

University of Windsor

Scholarship at UWindor

Electronic Theses and Dissertations

Theses, Dissertations, and Major Papers

7-7-2020

Developing highly symmetric Microelectromechanical systems (MEMS) based butterfly gyroscopes

Nabeel Ahmad Khan
University of Windsor

Follow this and additional works at: <https://scholar.uwindsor.ca/etd>

Recommended Citation

Khan, Nabeel Ahmad, "Developing highly symmetric Microelectromechanical systems (MEMS) based butterfly gyroscopes" (2020). *Electronic Theses and Dissertations*. 8376.
<https://scholar.uwindsor.ca/etd/8376>

This online database contains the full-text of PhD dissertations and Masters' theses of University of Windsor students from 1954 forward. These documents are made available for personal study and research purposes only, in accordance with the Canadian Copyright Act and the Creative Commons license—CC BY-NC-ND (Attribution, Non-Commercial, No Derivative Works). Under this license, works must always be attributed to the copyright holder (original author), cannot be used for any commercial purposes, and may not be altered. Any other use would require the permission of the copyright holder. Students may inquire about withdrawing their dissertation and/or thesis from this database. For additional inquiries, please contact the repository administrator via email (scholarship@uwindsor.ca) or by telephone at 519-253-3000ext. 3208.

Developing highly symmetric Microelectromechanical systems (MEMS) based butterfly gyroscopes

By

Nabeel Khan

A Thesis

Submitted to the Faculty of Graduate Studies
through the Department of Mechanical, Automotive and Materials Engineering
in Partial Fulfillment of the Requirements for
the Degree of Master of Applied Science at the
University of Windsor

Windsor, Ontario, Canada

© 2020 Nabeel Khan

Developing highly symmetric Microelectromechanical systems (MEMS) based butterfly gyroscopes

By

Nabeel Khan

APPROVED BY:

S. Alirezaee

Department of Electrical & Computer Engineering

V. Stoilov

Department of Mechanical, Automotive & Materials Engineering

J. Ahamed, Advisor

Department of Mechanical, Automotive & Materials Engineering

May 04, 2020

DECLARATION OF CO-AUTHORSHIP/PREVIOUS PUBLICATION

I. Co-Authorship

I hereby declare that this thesis incorporates material that is result of joint research of the author and his supervisor Prof. Jalal Ahamed. In all cases, the key ideas, primary contributions, experimental designs, data analysis, interpretation, and writing were performed by the author. The contribution of the professor included providing feedback on refinement of ideas and editing of the manuscript.

I am aware of the University of Windsor Senate Policy on Authorship and I certify that I have properly acknowledged the contribution of other researchers to my thesis, and have obtained written permission from each of the co-author(s) to include the above material(s) in my thesis.

I certify that, with the above qualification, this thesis, and the research to which it refers, is the product of my own work.

II. Previous Publication

This thesis includes 1 original paper that has been previously published/submitted for publication in peer reviewed journal, as follows:

Thesis Chapter	Publication	Publication Status
Chapter 2	N. Khan, M.J. Ahamed, "Design and development of a MEMS butterfly resonator using synchronizing beam and out of plane actuation," <i>Microsyst. Technol.</i> , vol. 26, no. 5, pp. 1643-1652, May 2020, https://doi.org/10.1007/s00542-019-04705-8	Journal (Published)

I certify that I have obtained a written permission from the copyright owners to include the above published material in my thesis. I certify that the above material describes work completed during my registration as a graduate student at the University of Windsor.

III. General

I declare that, to the best of my knowledge, my thesis does not infringe upon anyone's copyright nor violate any proprietary rights and that any ideas, techniques, quotations, or any other material from the work of other people included in my thesis, published or otherwise, are fully acknowledged in accordance with the standard referencing practices. Furthermore, to the extent that I have included copyrighted material that surpasses the bounds of fair dealing within the meaning of the Canada Copyright Act, I certify that I have obtained a written permission from the copyright owners to include such material in my thesis.

I declare that this is a true copy of my thesis, including any final revisions, as approved by my thesis committee and the Graduate Studies office, and that this thesis has not been submitted for a higher degree to any other University or Institution.

ABSTRACT

Microelectromechanical systems (MEMS) is the technology combining electrical components with mechanical systems at a micro scale. The combination of these two technologies allowed devices to interact with each other and build complex structures. System on the chips are built with components such as masses, electrodes, anchors, actuators and detectors. Reducing the size, weight, energy usage and cost is key while maintaining the sensors integrity. Sensitivity is an important factor when evaluating a gyroscope's performance. This research presents beam modeling techniques for maximizing mechanical sensitivity of the butterfly resonator for gyroscopic applications. It investigates the geometric aspects of synchronizing beam that connects the wings of a butterfly resonator. The results show that geometric variation in the synchronizing beam can have a large effect on the frequency split and sensitivity of the device. The model simulation demonstrates a sensitivity of 10^{-12} ($m/^\circ/s$) for a frequency split of 10 Hz, resulting from the optimized synchronous beam. Out of plane actuation was developed to drive and sense the resonators displacement. A butterfly sensor chip was fabricated to capture the dynamic responses of the resonator and to observe the theoretical and experimental results. Two butterfly resonators were tested, and the experimental results show a frequency split of 305 Hz and 400 Hz, while the model illustrated a split of 195 Hz and 220 Hz, respectively. The design and analysis presented in this thesis can further aid the development of MEMS butterfly resonators for inertial sensing applications.

DEDICATION

To my family, for their continuous support.

ACKNOWLEDGEMENTS

I would like to acknowledge the following people/organization for their assistance in completion of this thesis:

Dr. Jalal, for your support and guidance which helped me progress in the past two years. Thank you for the opportunity to work with you and keeping me motivated.

Dr. Li, for taking the time out and training me in how to use the SEM machine.

CMC Microsystems, for supporting me with this work, fabricating the sensor chip and providing me the necessary equipment and devices in a timely manner so I can complete the experimental portion of this research.

My research team at the MicroNano laboratory for their input and suggestions. This was a team effort which I was happy to be a part of.

TABLE OF CONTENTS

<i>DECLARATION OF CO-AUTHORSHIP/PREVIOUS PUBLICATION</i>	<i>iii</i>
<i>ABSTRACT</i>	<i>v</i>
<i>DEDICATION</i>	<i>vi</i>
<i>ACKNOWLEDGEMENTS</i>	<i>vii</i>
<i>LIST OF TABLES</i>	<i>x</i>
<i>LIST OF FIGURES</i>	<i>xi</i>
<i>Chapter 1</i>	<i>1</i>
Introduction	1
The Coriolis Effect	2
MEMS Vibratory Gyroscope	3
Literature Review	6
Objectives.....	13
Motivation	13
<i>Chapter 2</i>	<i>15</i>
Numerical Modeling	15
Mesh Independence.....	20
Geometric Parameter Variation.....	21
Sensitivity Analysis.....	26
Comb Drive Actuation	31
Stationary Analysis	35
Damping	42
Frequency Response.....	45
<i>Chapter 3</i>	<i>48</i>
Prototype Fabrication	48
PolyMUMPS Process.....	50
Design Layout	53
<i>Chapter 4</i>	<i>59</i>

Experimental Analysis	59
Apparatus Used	59
Breadboard Electronics	61
Test Setup	65
Probe Station	67
Response Plots.....	69
<i>Chapter 5</i>	73
Conclusion.....	73
Future Work	76
References	77
Vita Auctoris	81

LIST OF TABLES

Table 1. List of design parameters investigated as shown in Figure 15.....	21
Table 2. Optimized butterfly gyro dimensions using eigenfrequency model.	25
Table 3. Sensitivity parameters with their given values.....	28
Table 4. Sensitivity data with various drive and sense frequencies.	29
Table 5. Drive and sense force parameters with their given values.	35
Table 6. Parameter values used to calculate pull-in voltage.	41
Table 7. Parameter values used to calculate Q due to air pressure.	44
Table 8. Frequency summary for the three different studies.....	73

LIST OF FIGURES

Figure 1. A mass moving in direction v with an external angular input produces a perpendicular Coriolis force.	3
Figure 2. Linear vibratory rate gyroscope with two free orthogonal directions in which the proof mass oscillates. Adapted from [4].....	4
Figure 3. Working principle of a butterfly gyroscope using oscillating mass.	5
Figure 4. Prototype of the first butterfly gyro developed by IMEGO Institute in 1999. Adapted from [17].	7
Figure 5. Butterfly structure optimized for temperature robustness using spring absorbers. Adapted from [18].....	9
Figure 6. Dual-butterfly gyroscope with diamond shaped coupling mechanism. Adapted from [19].....	10
Figure 7. Butterfly-gyro using two large proof masses with a narrow central beam. Adapted from [20].	11
Figure 8. A butterfly’s antennae are attached to its head, which help provide flight stability during aerial maneuvers.....	14
Figure 9. Schematic design of a butterfly gyro showing the major components.....	16
Figure 10. Butterfly gyro model highlighted in blue as fixed constraint representing the anchors.	17
Figure 11. The first mode is the torsion of the synchronizing beam where the structure oscillates in phase at 6.55 kHz.....	18
Figure 12. The second mode is the torsion of the synchronizing beam with the proof masses oscillating 180° out of phase at 7.98 kHz.	18

Figure 13. The third mode is the lateral bending of the synchronizing beam with the proof masses oscillating out of phase at 7.97 kHz. 19

Figure 14. The fourth mode is the lateral bending of the synchronizing beam where the structure oscillates in phase at 13.2 kHz..... 19

Figure 15. Convergence curve showing optimum mesh configuration where the solution is mesh independent. 20

Figure 16. Schematic design showing the location of the geometric parameters studied. 21

Figure 17. Variation of proof mass dimensions and frequency split showing optimum value at 400 μm 22

Figure 18. Frequency split with synchronizing beam width showing optimum value at 9 μm . .. 23

Figure 19. Frequency split with paddle width showing optimum values of paddle beam size and asymmetry for minimum split..... 23

Figure 20. Frequency split with paddle length showing optimum value at 150 μm 24

Figure 21. Frequency split with paddle distance showing optimum value at 450 μm 25

Figure 22. The sense-mode system with an amplitude of 1000 and resonant frequency of 10.0 kHz, illustrating a 29% gain drop from a 5 Hz relative shift between the operating frequency and sense-mode resonant frequency. Adapted from [4]. 26

Figure 23. The amplitude provides a higher gain but is more sensitive to frequency variations. Resonant frequency for the sense-mode system is 10 kHz with Q of 10,000. A 5 Hz shift results in 90% gain drop. Adapted from [4]. 27

Figure 24. Sample calculations for two drive and sense frequencies illustrating a higher sensitivity with S_2 having lower split. 29

Figure 25. Sensitivity decreases with an increase in frequency split. Sensitivity is the ratio between vertical displacement and the rate of rotation..... 31

Figure 26. Cut-out view of proof mass in grey and electrodes in green. The proof mass has a floating potential node while the electrodes have bias voltage applied to them..... 32

Figure 27. Drive force vs electrode length showing an increase in electrostatic force as lateral distance (d) decreases. 34

Figure 28. Drive force vs electrode length showing an increase in drive force as the number of electrodes in the array are increased. 34

Figure 29. Electrostatic actuation and sensing model of butterfly gyroscope. This includes the nitride layer (in purple), fixed electrodes, butterfly resonator and air domain (not shown)..... 36

Figure 30. Butterfly gyro model with highlighted electrodes and anchors as fixed constraint. .. 37

Figure 31. Schematic of voltages applied to the electrodes underneath the proof mass. The drive electrodes include a DC bias potential that oscillates the proof mass into resonance. 37

Figure 32. Electric potential surface plot showing (a) drive mode gyro displacement and (b) corresponding orthogonal sense mode displacement..... 38

Figure 33. Displacement in the sense axis as a function of electric potential with a maximum of 26 nm. 39

Figure 34. Capacitance as a function of electrode gap showing an increase as the gap is reduced from 10 to 1 μm 42

Figure 35. Pressure vs Quality factor for the butterfly gyro, illustrating an increase in Q as the pressure decreases. 45

Figure 36. Frequency response from the simulated model showing multiple peaks under linear drive conditions. The ones of interest are located around 8 kHz with maximum amplitude corresponding to sense mode. 46

Figure 37. Zoomed view of the drive and sense mode operating frequencies at 8.11 and 8.33 kHz, respectively..... 47

Figure 38. Cross sectional view depicting the 7 layers of the PolyMUMPS process. Adapted from [35]. 49

Figure 39. Cross-sections depicting the PolyMUMPS fabrication process steps for the proposed butterfly gyro. 50

Figure 40. Cross-sections depicting PolyMUMPS fabrication process steps for the proposed butterfly gyro (cont.). 51

Figure 41. Photolithography process during exposure of photoresist using a positive tone, where exposed areas are being removed to etch the underlying structural layers. 52

Figure 42. 2D butterfly gyro drawn in L-Edit showing the location of bond pads and connections. 54

Figure 43. Bonding diagram of the butterfly chip illustrating a total of nine gyros with their respective bond pads and connecting electrodes. 56

Figure 44. Fabricated butterfly gyro showing (a) a SEM image of one chip and (b) the corresponding packaged gyroscope. 58

Figure 45. Frequency response test setup that includes two DC power supplies, a waveform generator, a spectrum analyzer, an oscilloscope and a breadboard to interface with the chip. 60

Figure 46. Actuation circuit where $I_A = AD620$, $R_G = 500k\Omega$, $R_1 = 1K\Omega$ and $C_1 = 1\mu F$ 62

Figure 47. Actuation circuit completed on the breadboard using amplifiers, resistors and capacitors.	63
Figure 48. Detection circuit where OA = OP177, IA = AD620, $R_G = 500k\Omega$, $R_F = 10k\Omega$ and $C_F = 10pF$	64
Figure 49. Breadboard implementation illustrating actuation, capacitive detection and MEMS device.	65
Figure 50. Setup of equipment and connections for the MEMS device.	66
Figure 51. Butterfly chip wire bonded from the bond pads to the outer contact pads.	67
Figure 52. Portable probe station with four positioners, digital microscope camera and butterfly chip sitting on top of the chuck.	68
Figure 53. Needles electrically probing the bond pads that are connected to the electrodes.	69
Figure 54. Frequency response of prototype 1 showing (a) drive and (b) sense mode at 8.495 kHz and 8.8 kHz.	71
Figure 55. Frequency response of prototype 2 showing drive mode frequency (a) at 8.6 kHz and sense mode frequency (b) at 9.0 kHz.	72

Chapter 1

Introduction

Microelectromechanical Systems (MEMS) are the combination of electrical components with mechanical systems at the micrometer ($1\mu\text{m} = 10^{-6}\text{m}$) scale. This combination of two technologies allows devices to interact with each other and build complex structures [1]–[3]. The chip's systems can be built from masses, flexures, actuators, detectors and gears [4]. Reducing the size and weight of these devices reduces the cost substantially [4]. Inertial sensors such as accelerometers, gyroscopes and inertial measurement units (IMUs) are finding significant applications in consumer electronics, automotive, aerospace and robotics technologies.

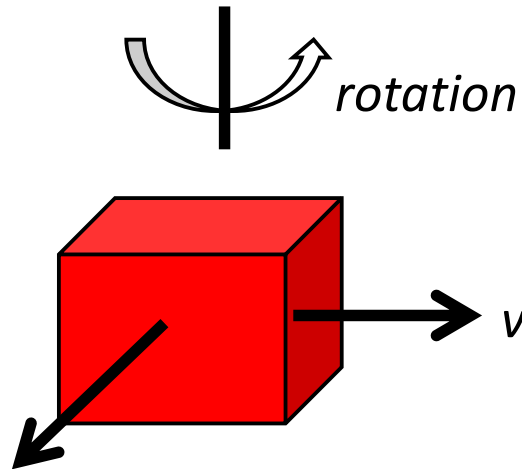
A gyroscope is a sensor that measures an object's rate of rotation [4]. A classical rotating wheel gyroscope is typically mounted on a gimbal structure with a rotating disc attached to an axle. The disc spins freely on its own axis and, when rotation is applied to the gimbal structure, the axis of rotation is unaffected. When subjected to rotation which resists any changes to the spinning disc orientation, a resistive force appears in the form of a Coriolis force. An IMU is a specific type of sensor that measures angular rate, linear acceleration and magnetic field. They are composed of a 3-axis accelerometer, 3-axis gyroscope and 3-axis magnetometer, resulting in a 9-axis IMU. This technology combines data from multiple sensors to measure orientation and heading [5].

The Coriolis Effect

The Coriolis force was first expressed in mathematics by Gaspard Gustave Coriolis in his paper titled, “*Mémoire sur les équations du mouvement relatif des systèmes de corps*” [6]. The Coriolis force acts on moving bodies rotating with respect to an inertial frame. The Coriolis force is shown in equation (1) where m is the mass, $\vec{\omega}$ is the angular velocity vector of the rotating frame and \vec{V} is the velocity vector with respect to the rotating reference frame.

$$\vec{F}_c = -2m (\vec{\omega} \times \vec{V}) \quad (1)$$

Inertial frame of reference is when objects are moving at a constant velocity or at rest with respect to Earth. This is the spatial position for an observer who is not accelerating. A clockwise rotation on a moving body forces the object to move left in its reference frame. An anticlockwise rotation causes the moving object to displace right. The deflection of the object is due to the Coriolis force is known as the Coriolis Effect. The Coriolis force is proportional to the rotation rate and the velocity of the body in the rotating frame, illustrated graphically in **Figure 1**.



$$\vec{F}_c = -2m (\vec{\omega} \times \vec{V})$$

Figure 1. A mass moving in direction v with an external angular input produces a perpendicular Coriolis force.

The force acts in the direction perpendicular to the rotation axis and the body in the rotating frame. It can be found by using the right-hand rule. This force only exists in an accelerating frame of reference where a body is experiencing motion. With an inertial frame of reference, i.e. at rest, the Coriolis force disappears. The acceleration of the Coriolis force is a result of the object's velocity changing with time. As the object is in motion within a rotating reference frame, the velocities are different at a given time. Within the rotating reference frame, the velocities are also different in respect to position seen from a fixed reference frame.

MEMS Vibratory Gyroscope

Gyroscopes are sensors that measure an object's rate of rotation. MEMS gyroscopes are miniature motion sensors. The majority of reported micromachined gyroscopes use vibrating mechanical elements to sense angular rate [4], [7]–[9]. Compared to classical rotating wheel gyroscopes, MEMS gyroscopes have several advantages, as there are no more rotating parts, eliminating

friction. Due to a combination of resonating proof mass and an orthogonal angular-rate input, these micromachined gyroscopes use sinusoidal Coriolis force [4]. **Figure 2** shows a generic MEMS linear vibratory gyroscope, where the proof mass is free to oscillate in two orthogonal directions.

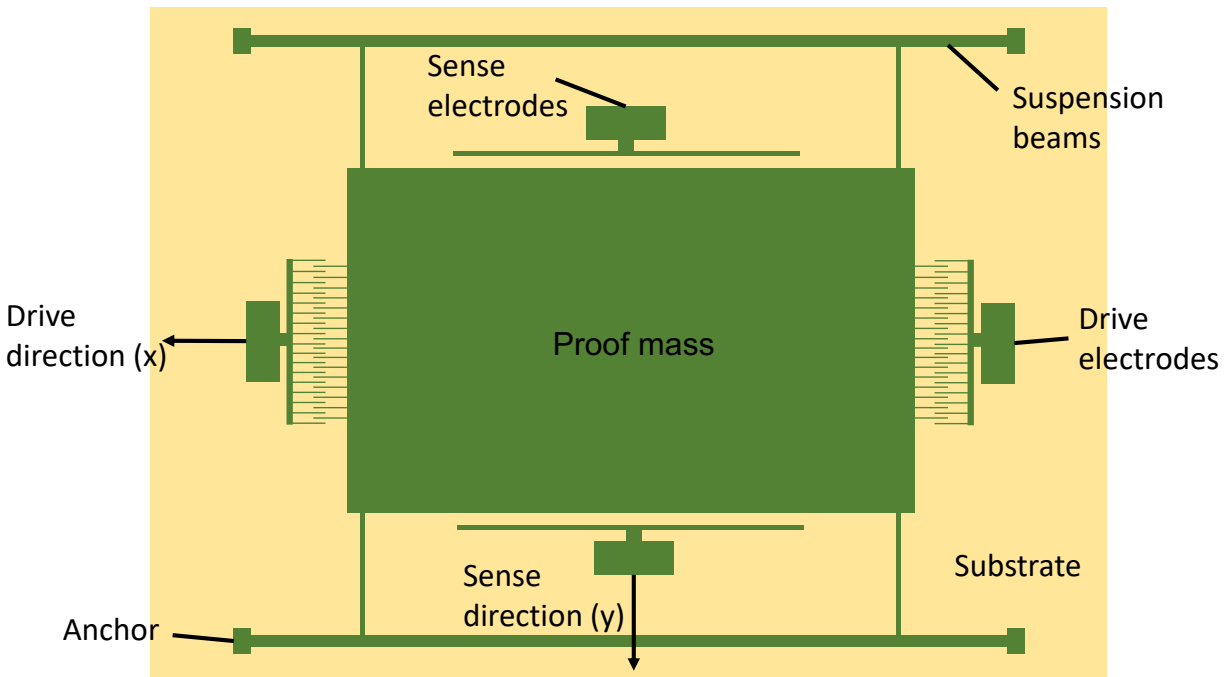


Figure 2. Linear vibratory rate gyroscope with two free orthogonal directions in which the proof mass oscillates. Adapted from [4].

The structure of the gyroscope is suspended above the substrate so it's free to move during the drive and sense modes of operation. The Coriolis force causes an energy transfer from the drive mode oscillator to the sense mode proportional to the angular rate input [4]. The drive mode oscillator is usually an external sinusoidal electrostatic force at a certain frequency. This frequency, known as the drive frequency, must match the sense mode frequency. Applying an external angular rate produces a sinusoidal Coriolis force at the driving frequency. The direction of the force is orthogonal to the drive mode oscillator and angular rate input [4].

The butterfly gyro works in the same manner. Instead of one or two proof masses, there are usually four proof masses [10]–[12]. The masses are made to oscillate by an external force at the drive frequency in the drive direction.

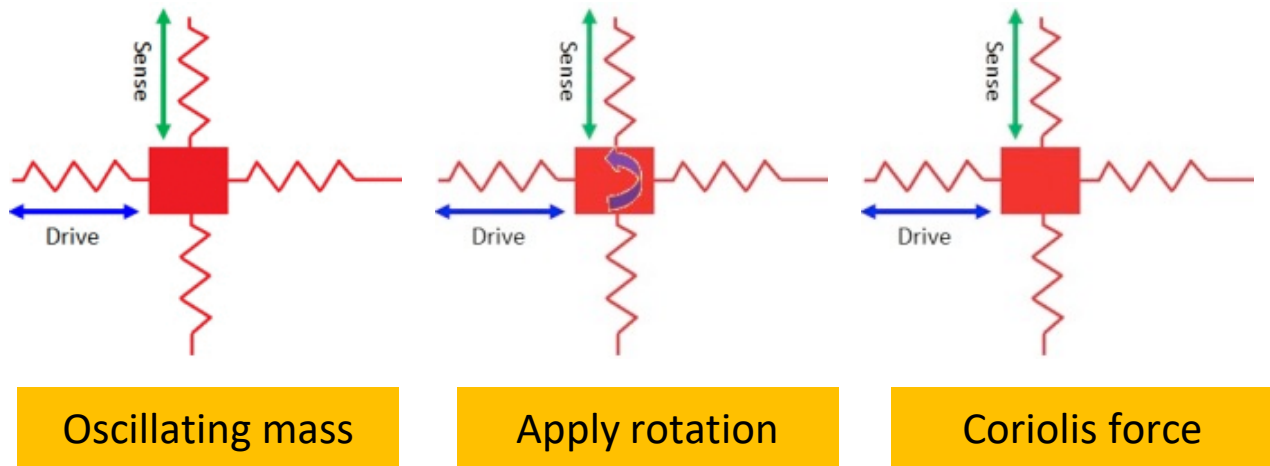


Figure 3. Working principle of a butterfly gyroscope using oscillating mass.

When a rotation is applied orthogonally, there is displacement induced by the Coriolis force, which is perpendicular to the oscillating motion and applied rotation shown in **Figure 3**. External electrostatic forces are used to drive the proof masses into oscillation. Electrodes are placed underneath the structure to sense the orthogonal displacement due to the Coriolis force. There is an initial capacitance between the proof mass and electrodes, but, as the proof mass displaces, the capacitance changes. This information is then fed back into a controller to extract the amount of rotation incurred.

MEMS gyroscopes are constantly improving and are preferred over bulky conventional gyroscopes [13], [14]. Conventional gyroscopes have many moving parts that result in friction, thus hindering performance. There are high-precision sensors, such as fiber-optic and ring laser gyroscopes, but these are too expensive for emerging applications [4], [15]. Micromachining

processes allow for the batch production of MEMS devices, reducing unit cost and attracting the inertial market. Advances in manufacturing techniques is leading to the complex integration of electronics and mechanical sensor elements on silicon chips. MEMS gyroscopes have an array of applications in the aerospace industry, the military, the automotive industry, consumer electronics, biomedical/health, and safety. This includes automotive safety systems, such as electronic stability control (ESC) [4], high precision and guidance systems, ride stabilization, and image stabilization in cell phone cameras, as well as uses in the gaming industry and in virtual reality products.

The MEMS gyroscope devices are usually manufactured using photolithography-based semiconductor fabrication techniques at the micro scale. This technology for making semiconductors allows the building of moving micro-structures from either a top-down or bottom-up approach. The top-down approach starts from a solid unit of material. The material is etched from the top down until the desired shape and size are reached. The bottom-up method starts on the substrate. Materials are then added and stacked onto each other, resulting in the desired final product. The advantage of the top-down approach is the “ability to put the desired feature in an exact location.” This is limited, however, by the resolution of the cutting tool technology [16]. Similarly, the bottom-up method is able to produce devices in a large scale, but controlling the features can become difficult.

Literature Review

There are several types of gyroscopes, including mechanical, MEMS and optical. Mechanical gyroscopes use a rotating momentum wheel or disc to maintain orientation. The disadvantages of these type of gyros primarily concern friction and wear [4]. MEMS gyros, such as the

Hemispherical Resonator Gyroscope (HRG) and Tuning-Fork Gyroscopes, use micromachining processes to build the resonating structure at the micron scale. These gyros remove the bearing problems by eliminating rotating parts. Optical gyroscopes, such as fiber-optic and ring laser gyros, are able to get rid of virtually all mechanical limitations [4]. Their ability to remove all vibrations, friction and rotating parts has led to their usage in high-end applications. The focus of this research is the MEMS butterfly gyroscope. Multiple research papers were used in the gathering of information. From previous research, data was collected on the work that currently exist. A topic was then selected to address a problem different than what others have investigated.

The first research paper reviewed was the original paper on the butterfly gyro, published in 1999 [17]. This gyro had single-sided electrostatic excitation and capacitive detection. It had four proof masses vibrating in anti-phase shown in **Figure 4**, so the offset is smaller and the gyro is less sensitive to linear and angular vibration [17].

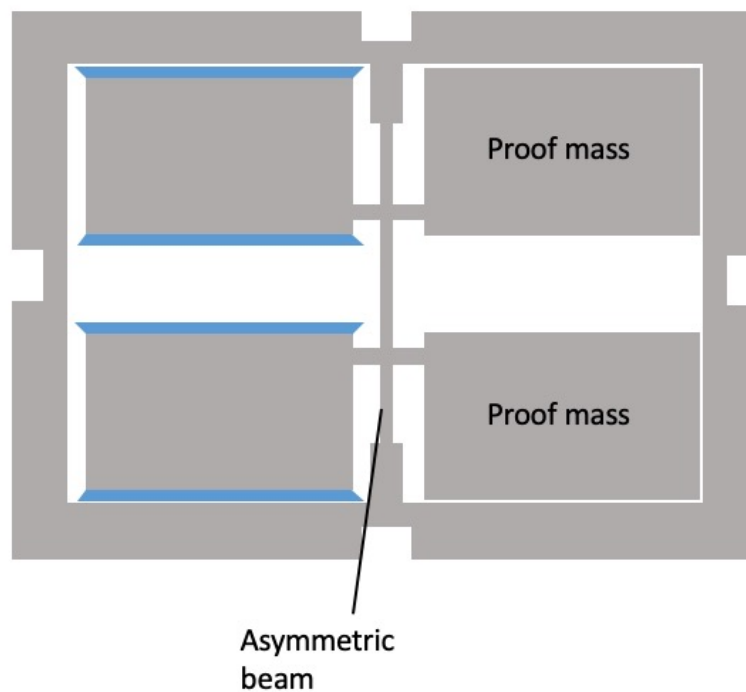


Figure 4. Prototype of the first butterfly gyro developed by IMEGO Institute in 1999. Adapted from [17].

The gyro was operated at atmospheric pressure and had a sample resolution of 0.1 at 50 Hz bandwidth [17]. The working principle of this gyro included an asymmetric central beam that bent vertically and horizontally when induced with vertical electrostatic forces. The masses vibrated horizontally and, when a rotation was applied, produced vertical Coriolis forces which were capacitively detected. The main source of damping in this design was the squeezed-film damping, as the electrode gap was 5 μm [17]. This butterfly gyro was made using anisotropic etch and double-sided patterning of the oxidized silicon wafer [17]. There was a glass wafer anodically bonded to the silicon where the silicon electrodes were placed. This gyro was intended for roll-over application with a full-scale range of $\pm 250^\circ/\text{s}$ [17]. This research established the concepts for the butterfly gyro, but there needs to be continued development to reduce the size and cost of the chip.

The second paper reviewed focused on the temperature-robust design of the butterfly gyro [18]. Sensors have a reliability problem where thermal stresses have caused a wide range of temperature distribution. There is a mismatch of the thermal expansion coefficients between the silicon structure and glass substrate [18]. This temperature affects the device's performance, reducing robustness and stability. With the butterfly gyro, this happens at the central beam, where there is a fixed constraint at both ends. Linear or torsional motion causes internal stress at the anchor points. This research proposed that the fixed ends include a spring absorber to reduce the internal stress, thus reducing the temperature variation shown in **Figure 5**.

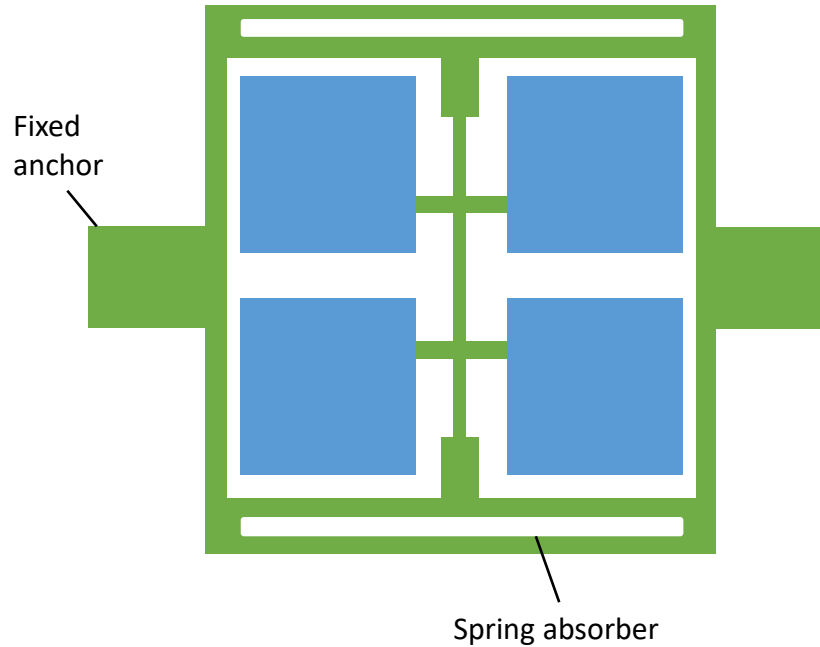


Figure 5. Butterfly structure optimized for temperature robustness using spring absorbers. Adapted from [18].

The research goes on to state that the frequency split was between 350 to 400 Hz [18]. Before tuning the gyro, the results showed that, for the drive and sense modes of operation, the resonant frequency decreased by 0.41 Hz/degC and 0.12 Hz/degC respectively [18]. The non-tuned structure's frequency split was 29.3 Hz [18]. When the butterfly gyro was tuned, the variation of resonant frequency decreased from 41.3 Hz to 16 Hz with an ambient temperature ranging from -40 to 60 °C [18]. The frequency split decreased to 3.81 Hz [18]. This paper demonstrated a temperature-robust design that used a spring absorber for a more flexible approach to clamped end resonators.

The third paper reviewed was titled “A Dual-Butterfly Structure Gyroscope” [19]. This research took a traditional butterfly gyroscope and added another butterfly structure, with each of the gyros having their own central beam. The gyroscope had a mechanism to couple two single butterfly structures and keep the driving mode phase of the gyroscopes opposite [19]. This had the advantage

of improving the bias instability and g-sensitivity [19]. The coupling mechanism was diamond-shaped with folded springs at its end to reduce internal stress, as shown in **Figure 6**.

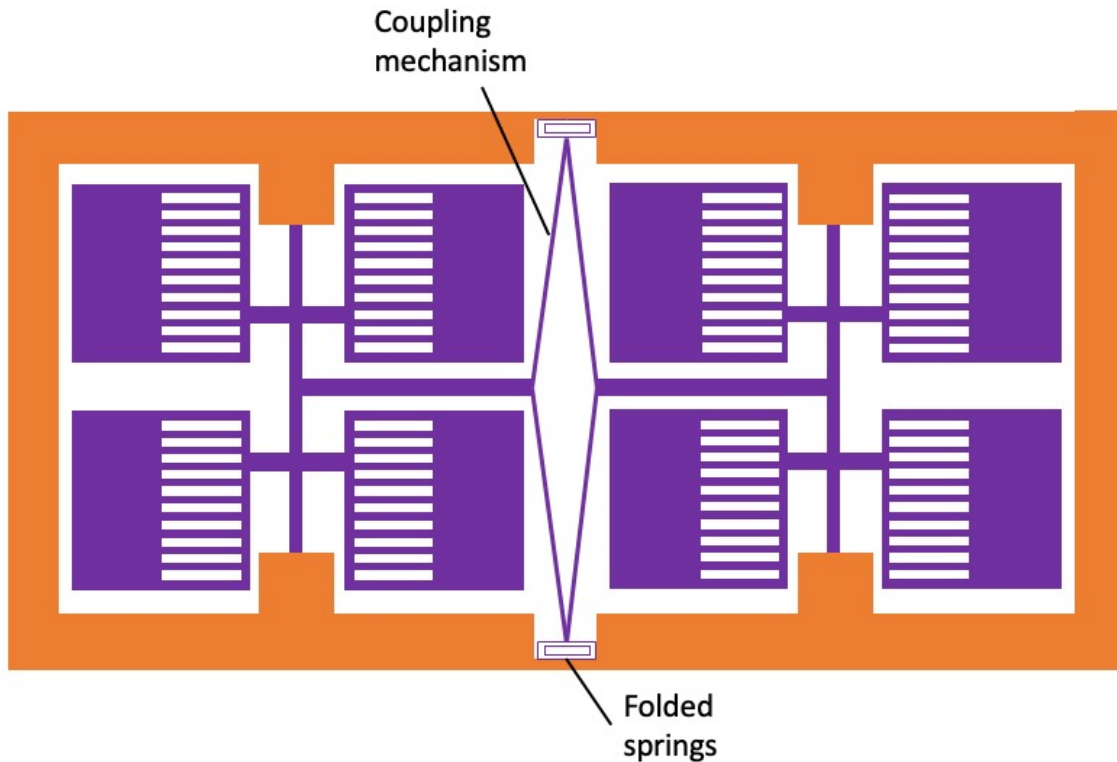


Figure 6. Dual-butterfly gyroscope with diamond shaped coupling mechanism. Adapted from [19].

The coupling mechanism makes the in-phase frequency much higher than anti-phase frequency, which receives less influence from low-frequency environmental noise [19]. The eigenfrequency in the drive and sense modes were 3,914.5 Hz and 4,190.7 Hz, respectively. The dry etching method was used to create a rectangle-shaped central beam, which used tangential driving force to increase the vibration amplitude of the gyro. The overall gyro structure has a 10 mm x 18 mm dimension and is vacuum-sealed under a pressure of 10^{-6} Pa [19]. The experimental results showed a Q-factor of 10,967 in the drive mode condition, a scale factor of 10.9 mV/°/s and a bias instability of 10.7 °/h [19]. This research paper illustrated the design and simulation of a dual butterfly gyro using a coupling mechanism to increase the in-phase mode frequency.

The fourth research paper studied was titled “Bulk Micromachined Angular Rate Sensor based on the Butterfly-Gyro Structure” [20]. In this paper, three layers of glass, silicon and glass were used for the structure where bulk silicon was anodically bonded. This butterfly gyro structure used asymmetric beams and plate electrodes. It needed beams that were “high and narrow with a certain asymmetry in the cross section” [20]. The central beams were rectangular in shape and bent 5° from the horizontal plane [20]. The excitation forces bent the central beam both vertically and horizontally. This butterfly gyro used two large masses instead of the four shown in **Figure 7**. The vibrating masses move 180° , out of phase with each other [20].

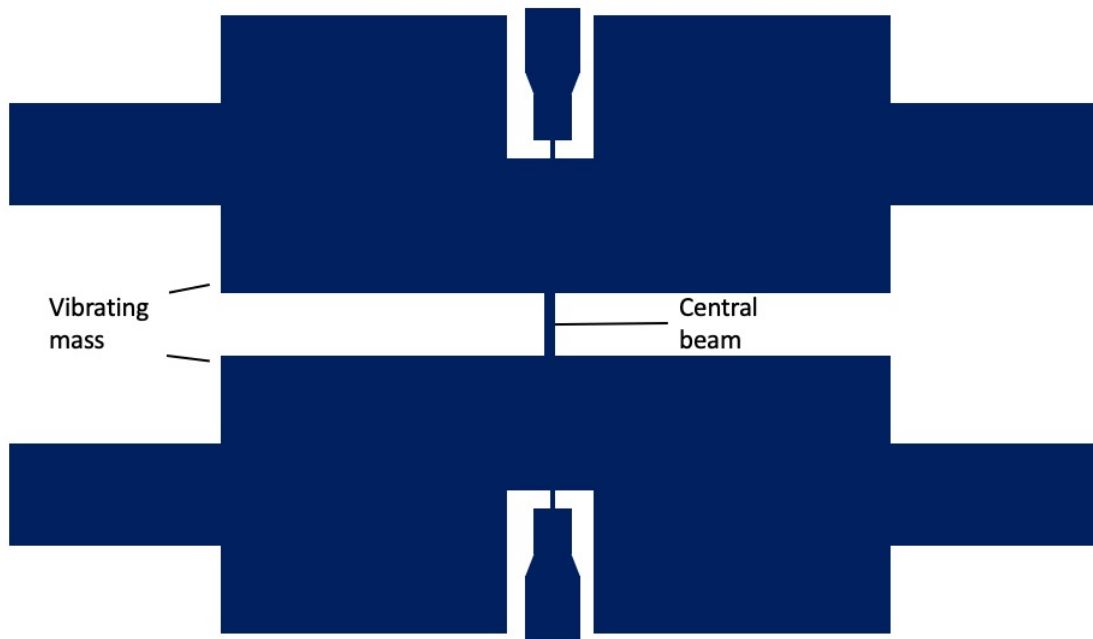


Figure 7. Butterfly-gyro using two large proof masses with a narrow central beam. Adapted from [20].

The drive and sense modes of operation were at 9.0 kHz and 9.3 kHz, respectively. The silicon structure included holes to reduce the damping effects and increase Q-factor. A 1.0 mm electrode gap was formed by dry etching the silicon [20]. The Q-factor was 170,000 for the excitation mode and 1,600 for the detection mode [20]. The scale factor was $77 \text{ mV}/^\circ/\text{s}$ and the shock survivability

was above 10,000 G [20]. This research investigated an alternative design for the butterfly gyro with a bulk micromachined process using a single crystalline silicon.

The following studies have been carried out from previous research:

1. Coupling two single butterfly gyroscopes using a spring mechanism to reduce damping effects.
2. Butterfly gyro using a spring absorber design to reduce frequency split across a range of temperatures.
3. A unique gyro design where two large proof masses have been used rather than the traditional four smaller proof masses.
4. Using an oblique beam to generate horizontal driving forces and vertical Coriolis forces, which are capacitively detected.
5. Using horizontal driving force to improve the scale factor.

The goal of this research is to improve sensitivity using structural optimization by reducing the frequency split. The research's focus is the influence of the beam asymmetries on the mechanical sensitivity of the butterfly resonator. Analytical sensitivity and force calculations have been evaluated to characterize this gyro. A butterfly resonator model has been developed to capture the frequency and mode shape. The analyses here are important because reduction in the frequency split increases sensitivity and leads to a superior device.

Objectives

The purpose of this thesis is to explore several aspects of the butterfly gyroscope. This includes optimizing the geometric parameters to reduce frequency split. In turn, this will improve the sensitivity of the resonator. Finite element modeling techniques are used to estimate the mode shapes and corresponding frequencies. Next, a fabrication platform is selected based on the requirements of the butterfly gyro. Finally, experimental validation is carried out to compare the accuracy of the theoretical models.

The geometric parameter variation is studied in order to structurally optimize the gyroscope. The optimized parameter is the frequency split. The drive and sense frequencies are needed close to each other in order to reduce the split. This is done by creating a model and running an eigenfrequency study. The sensitivity is improved by a combination of variables. This includes the geometry, stiffness and frequency of the device. The modeled design has to follow the fabrication rules in order to manufacture the device; the rules are taken into consideration when modeling the sensor. The last step is to test the device against theoretical data and compare the findings.

Motivation

The motivation behind this research lies in nature. Flying insects have a pair of club-shaped organs on their bodies called halteres, which provides body rotation information during flight [21]. Insects such as crane flies, houseflies and mosquitoes possess halteres, and butterflies possess antennae, which operate in a way remarkably similar to halteres (**Figure 8**) [22].



Figure 8. A butterfly's antennae are attached to its head, which help provide flight stability during aerial maneuvers.

Halteres operate in a way analogous to a vibrating gyroscope. They oscillate rapidly along with the wings and any rotation of the plane of oscillation causes the halteres to displace by the Coriolis force. The insect detects this force using sensory organs located at the tip of the halteres and interprets this information, correcting its position in space [21]. The butterfly gyroscope works similarly, as there is an oscillating mass with an external rotation applied to it and the Coriolis force causing displacement.

Chapter 2

Numerical Modeling

A finite element model (FEM) was developed for the butterfly resonator to numerically simulate its operation, optimize geometric features by estimating performance matrix. The FEM model can divide a continuous 3D solid into many tetrahedrons composed of nodes and boundaries called meshing. This technique breaks an infinitely continuous physical object into a finite number of interacting boundaries [23]. After the FEM is designed, the finite element analysis (FEA) is carried out by defining the known boundary conditions and applying physics to the model. The FEA is important, as this reduces fabrication time due to errors in geometry and, in this day and age, complex models can be solved in an acceptable time frame. The FEA also aids in design, as one can refine their design repeatedly before prototyping and fabrication.

COMSOL Multiphysics is a powerful interactive software for solving engineering problems. It includes a desktop environment with multiple interfaces for building models. Multiphysics coupled models can be defined with physical quantities such as loads, constraints and material properties without having to define the underlying equations. Various studies can be performed using the physics interface, including transient, linear and frequency responses.

The first step in the analysis was to run an eigenfrequency study. The eigenfrequency study includes the eigenfrequencies and the eigenmodes of the vibrating structure. A generic butterfly geometry was drawn in COMSOL Multiphysics 5.3a. The eigenfrequencies correspond to the “natural frequencies of vibrations and the eigenmodes correspond[ed] to the normalized deformed

shapes at the eigenfrequencies” [24]. The first objective was to obtain the correct resonance mode shape, i.e. the eigenmodes. With the correct mode shape, the frequency would be tuned after. The frequency model was an iterative process where a geometry was drawn, then the study was computed and, finally, the geometry was tweaked in order to improve the performance. The first couple of studies computed had the geometry of a rudimentary butterfly structure.

The geometry consists of four proof masses, a synchronizing beam, two anchors and two paddle beams connecting the proof masses to the structure, as shown in **Figure 9**.

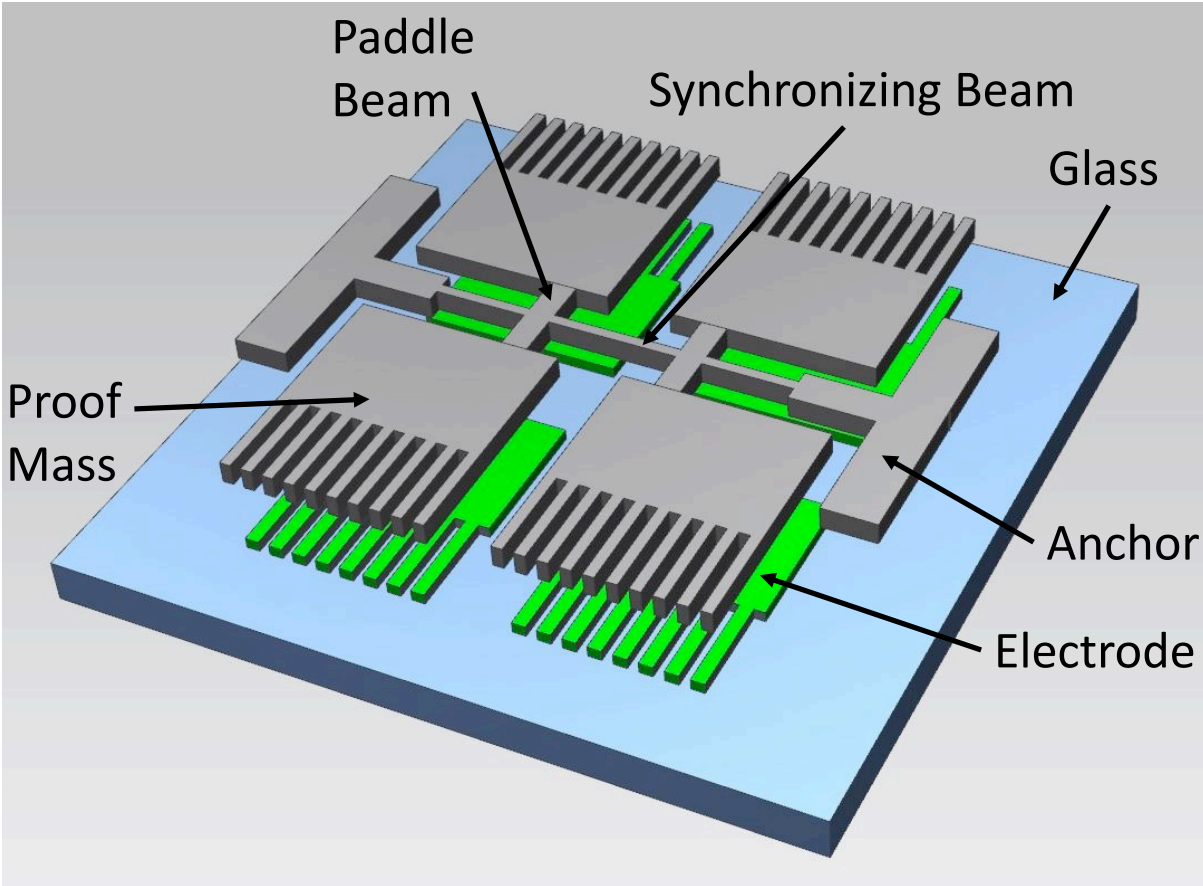
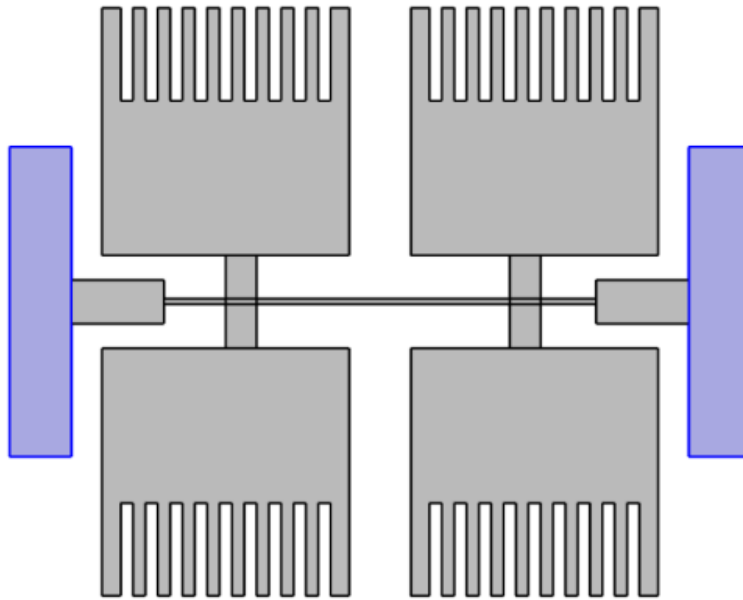


Figure 9. Schematic design of a butterfly gyro showing the major components.

Underneath the structure are electrodes, which sit on a glass substrate not modeled in the frequency study. Boundary conditions include the anchors being fixed while the rest of the structure is free to vibrate, as highlighted in **Figure 10**.



***Figure 10.** Butterfly gyro model highlighted in blue as fixed constraint representing the anchors.*

The iteration was carried out with a multivariable process. At any given geometry, two eigenmodes and eigenfrequencies were of interest concerning the drive and sense modes of operation. There were other distorted mode shapes and frequencies, but these were not useful in the analysis. When the correct eigenmodes were obtained, the geometry was tweaked in order to adjust the eigenfrequency. In the butterfly structure, the first mode is the torsion of the synchronizing beam, which oscillates the mass in phase at 180° , as illustrated in **Figure 11**. The second mode is also the torsion of the synchronizing beam, but the mass is oscillating out of phase at 180° , as illustrated in **Figure 12**. The third mode is the lateral bending of the synchronizing beam, making the mass oscillate 180° out of phase, as illustrated in **Figure 13**. The fourth mode is also the lateral bending of the synchronizing beam, but the mass oscillates 180° in phase, as illustrated in **Figure 14**. The

surface plot of the mode shapes below has been exaggerated for illustrative purposes. The blue in the images represents maximum displacement while the green represents minimum displacement.

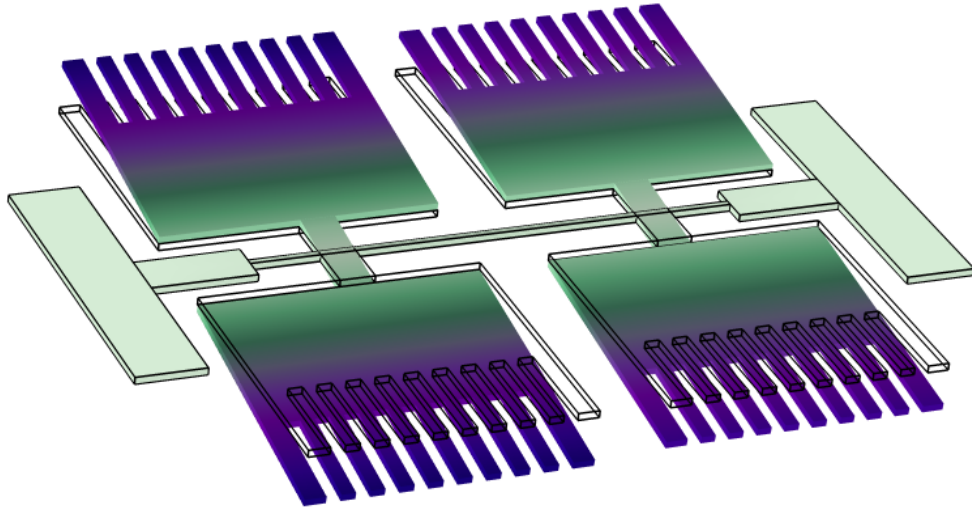


Figure 11. The first mode is the torsion of the synchronizing beam where the structure oscillates in phase at 6.55 kHz.

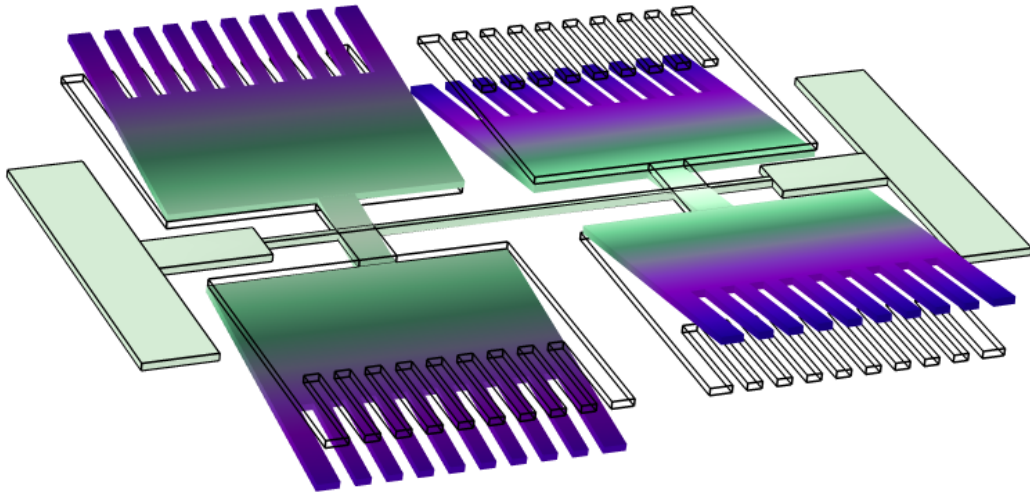


Figure 12. The second mode is the torsion of the synchronizing beam with the proof masses oscillating 180° out of phase at 7.98 kHz.

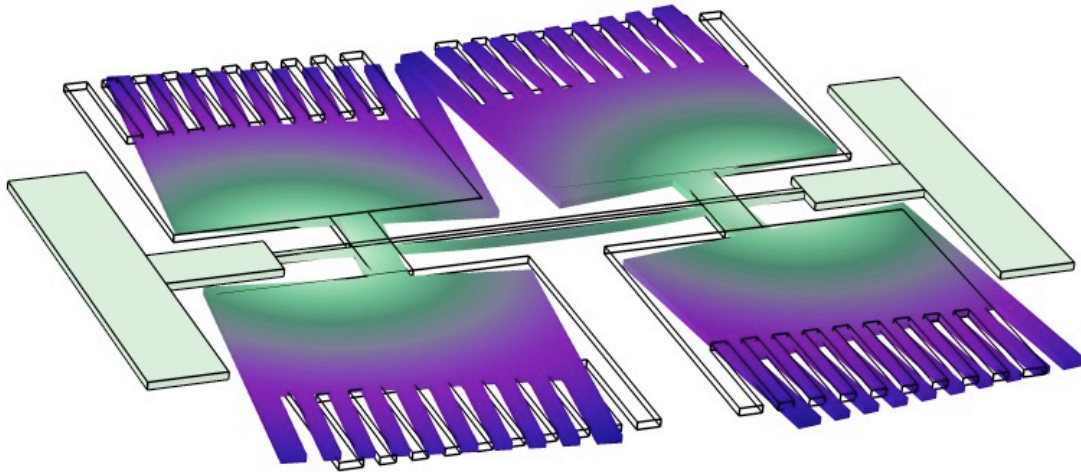


Figure 13. The third mode is the lateral bending of the synchronizing beam with the proof masses oscillating out of phase at 7.97 kHz.

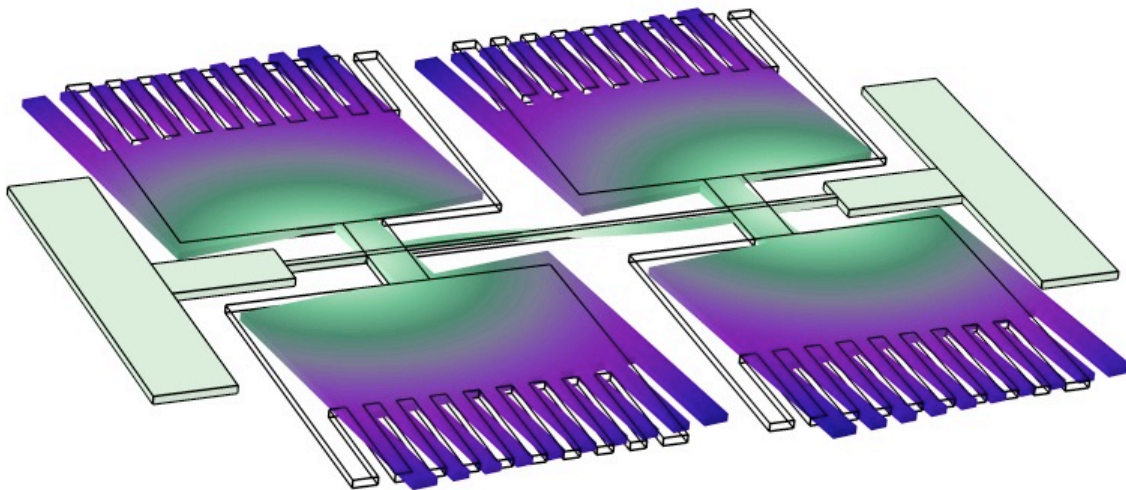


Figure 14. The fourth mode is the lateral bending of the synchronizing beam where the structure oscillates in phase at 13.2 kHz.

The second and third mode shapes are active in the sense and drive operations, respectively. The second (detection) mode senses the angular rate input and the third (excitation) mode is driven into resonance by electrostatic forces. After obtaining the correct mode shapes, shown in **Figure 12** and **Figure 13**, the geometry was tweaked in order to reduce the split between the drive and sense mode frequencies.

Mesh Independence

A mesh independence test was performed on the butterfly gyro to rule out error in the solution from meshing. This convergence helps to eliminate any influence from frequency and frequency split due to mesh size. The type of mesh element used in the model was tetrahedrons. The study began with the default physics-controlled mesh sequence and then the sequence was customized for a more accurate simulation. Adaptive mesh refinement was also used, in which the software solves with the initial mesh and iteratively inserts elements, re-solving the model.

The convergence curve in **Figure 15** shows that the eigenfrequency of the resonator converges at 7,921 Hz, with a mesh configuration of 186,000 elements. This was deemed acceptable for the analysis.

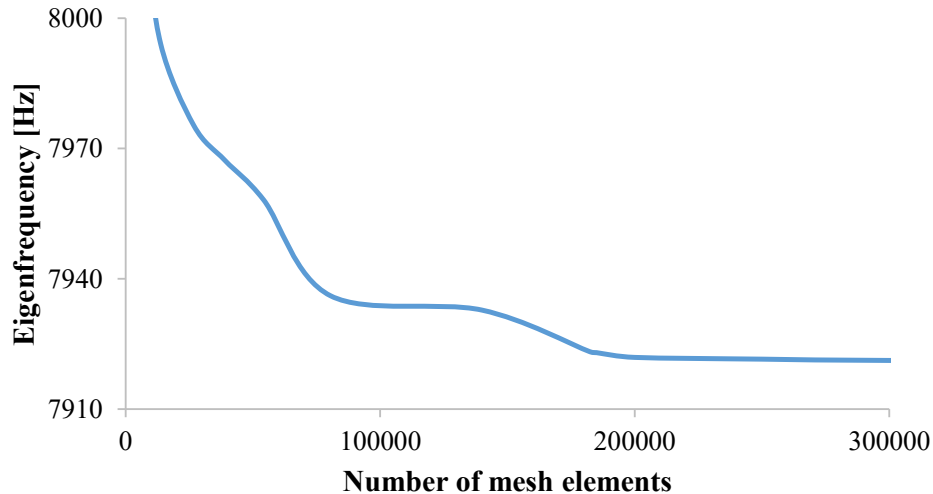


Figure 15. Convergence curve showing optimum mesh configuration where the solution is mesh independent.

Geometric Parameter Variation

Once a suitable mesh is established, a geometric parameter variation was performed to find out best geometry while maximizing performance. There were six geometric parameters that were varied, as shown in **Table 1**. Their respective location on the butterfly gyro is shown in **Figure 16**.

Table 1. List of design parameters investigated as shown in Figure 15.

Variable	Description
W	Width of proof mass
L	Length of proof mass
t	Width of synchronizing beam
H	Width of paddle beam
K	Distance from mass to beam
U	Distance between the paddle beams

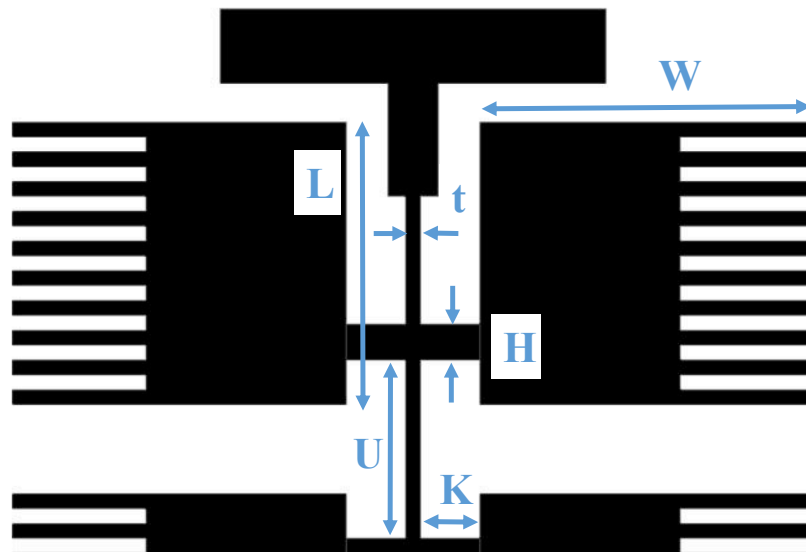


Figure 16. Schematic design showing the location of the geometric parameters studied.

The width of the proof mass “W,” length of the proof mass “L” and width/length are plotted against frequency split, as shown in **Figure 17**. The width was varied from 300 to 500 μm while keeping the length constant, then the length was varied while keeping the width constant and then both

were varied at the same time. It was noticed at 400 μm that varying both the length and width produced the lowest frequency split: 4.7 Hz.

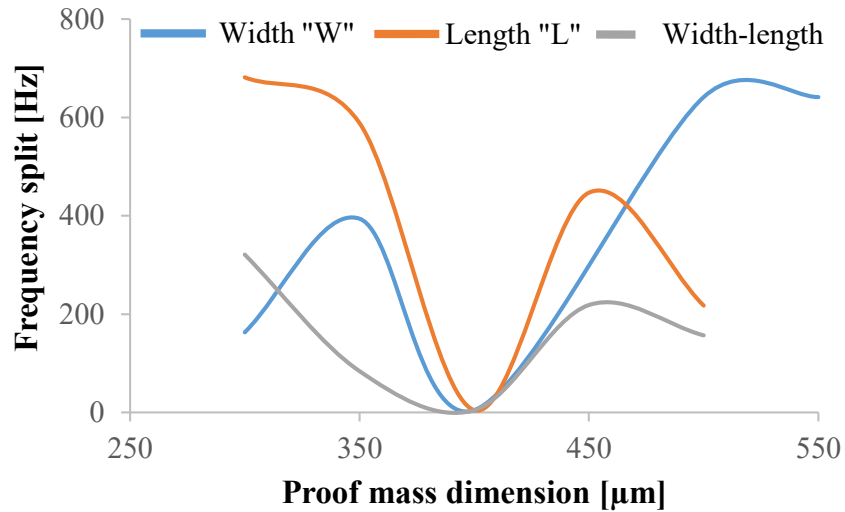


Figure 17. Variation of proof mass dimensions and frequency split showing optimum value at 400 μm .

The width of synchronizing beam “t” was also varied from 3 to 11 μm against frequency split shown in **Figure 18**. At 9 μm beam width, the frequency split was reduced to 7.3 Hz. The synchronizing beam was the most sensitive geometrical parameter when reducing the frequency split. Small deviations in the geometry resulted in considerable changes in the frequency split. This is illustrated by the wide range of frequency split on the vertical axis in **Figure 18**.

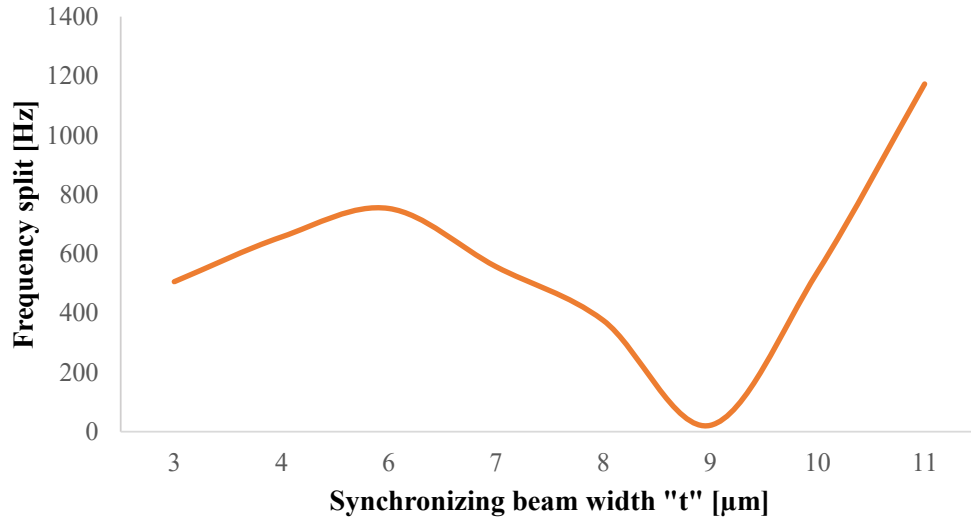


Figure 18. Frequency split with synchronizing beam width showing optimum value at 9 μm .

Next, the width of the paddle beam “H” was varied from 20 to 90 μm , as shown in **Figure 19**. At 45 μm , the frequency split was reduced to 4.7 Hz. This parameter was the least sensitive to variations in frequency split, as illustrated by the mere range of frequency split on the vertical axis in **Figure 19**.

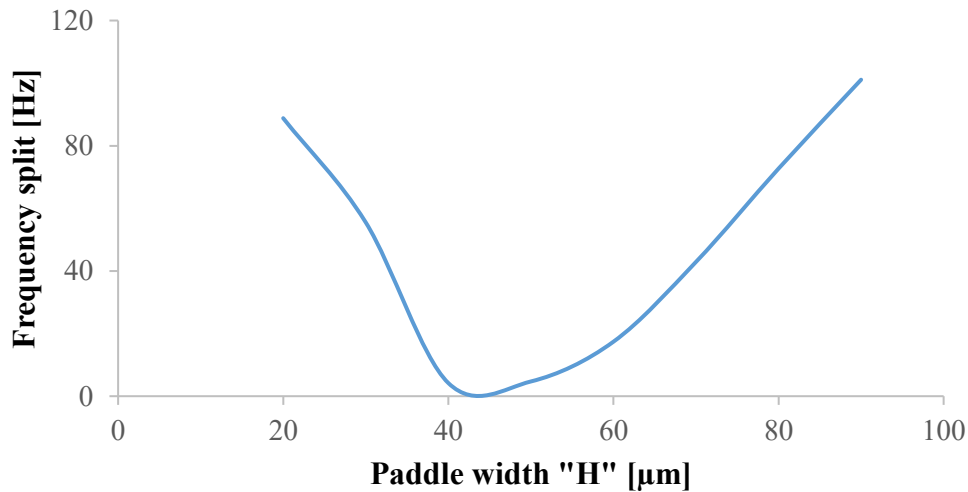


Figure 19. Frequency split with paddle width showing optimum values of paddle beam size and asymmetry for minimum split.

The next variable studied was “K,” the distance from the proof mass to the beam. This is essentially the length of the paddle beam from the edge of the synchronizing beam to the proof mass. This was varied from 120 to 175 μm , as shown in **Figure 20**. At 150 μm , the frequency split had reduced to 5 Hz.

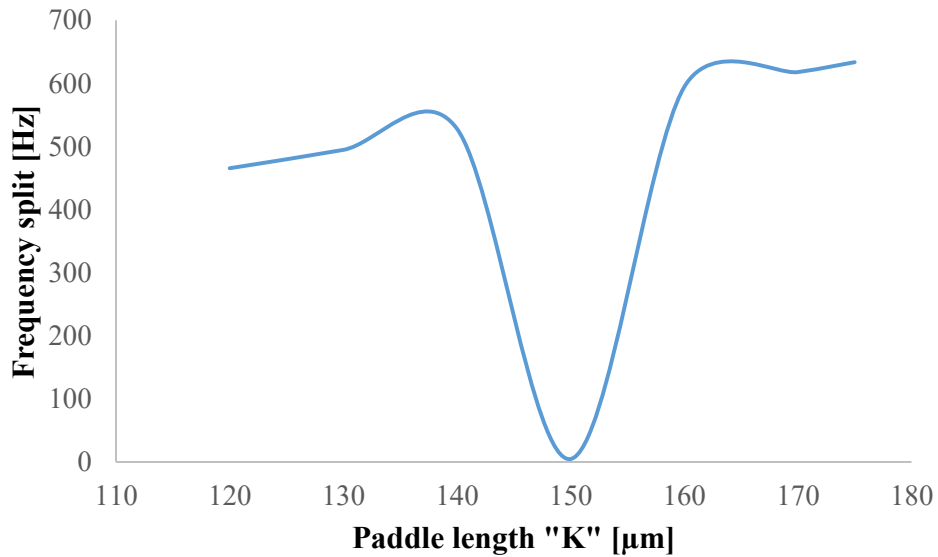


Figure 20. Frequency split with paddle length showing optimum value at 150 μm .

The last parameter studied was “U,” the distance between the paddle beams. This parameter determined what size the butterfly gyro would be. **Figure 21** illustrates the results; this parameter was varied from 250 to 550 μm . At 450 μm , it produced the lowest frequency split of 5 Hz.

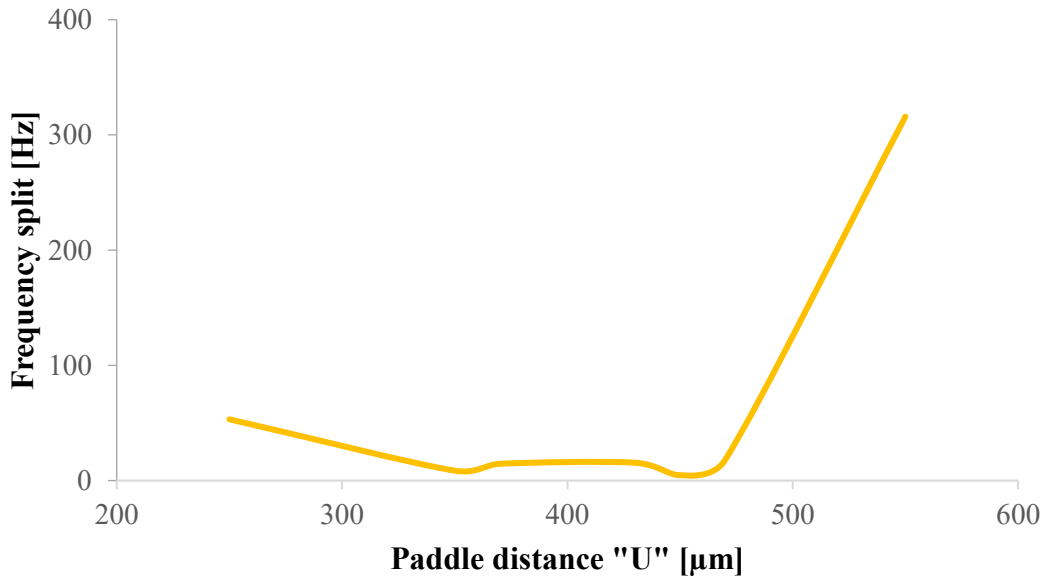


Figure 21. Frequency split with paddle distance showing optimum value at 450 μm .

Table 2 shows the final dimension of the optimized butterfly gyro with an overall size of 1 mm x 1 mm and a thickness of 10 μm . Rather than trying to optimize a single parameter, holding it constant and varying another parameter, a slightly different approach was used. Two or more parameters were varied in order to find the optimal range. All the parameters are dependent on each other when looking at the frequency and slight changes in the geometry can cause large deviations in the frequency and frequency split.

Table 2. Optimized butterfly gyro dimensions using eigenfrequency model.

Parameter	Value [μm]
Proof mass [W, L]	400
Distance between paddle beams [U]	450
Width of the paddle beam [H]	45
Distance between proof mass to synchronizing beam [K]	150
Width of synchronizing beam [t]	9
Overall gyro size	1x1 mm
Thickness of device	10

Sensitivity Analysis

The Coriolis Effect is based on the conservation of momentum, so gyroscopic systems need subsystems that generate momentum. The drive mode oscillator provides a sinusoidal drive-mode excitation force, which oscillates the system at the drive mode resonant frequency. The phase and frequency of drive oscillation directly determines the Coriolis force and the sense-mode response [4]. The drive and sense mode oscillators are both 1-DOF resonators. The Coriolis accelerometer excites the sense-mode oscillator at resonance to amplify the mechanical response of the Coriolis force. To achieve maximum gain in the sense-mode, it is desirable to operate at the peak of the sense-mode curve. This is accomplished by matching drive and sense resonant frequencies.

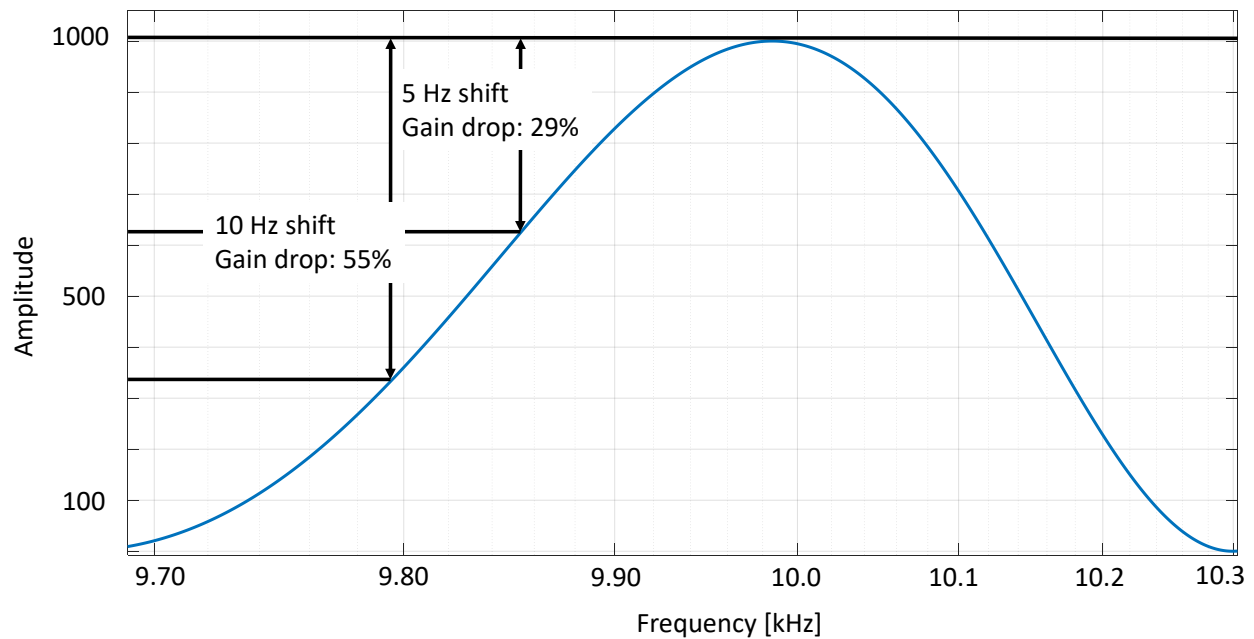


Figure 22. The sense-mode system with an amplitude of 1000 and resonant frequency of 10.0 kHz, illustrating a 29% gain drop from a 5 Hz relative shift between the operating frequency and sense-mode resonant frequency. Adapted from [4].

Figure 22 illustrates this effect in the sense mode system. The system's resonant frequency is 10 kHz with a Q of 1,000. When the operating frequency matches the sense-mode resonant frequency,

the amplification factor is 1,000, equaling the Q factor. If there is a 5 Hz difference between operating and sense-mode frequency, the gain drops by 29.3% [4]. The gain drops 55% with a 10 Hz relative shift [4]. When the Q factor is increased, the gain is higher but the bandwidth becomes narrower. For a resonant frequency of 10 kHz and Q of 10,000 (**Figure 23**), a 5 Hz shift has a 90% gain drop. A 10 Hz shift results in a 95% gain drop. The curve for the 10,000 Q is a lot sharper, but also more sensitive to variations in system parameters which can shift the resonant frequency. Fabrication imperfections, deposition conditions, fluctuations in the ambient temperature and stresses result in resonant frequency fluctuations during operation.

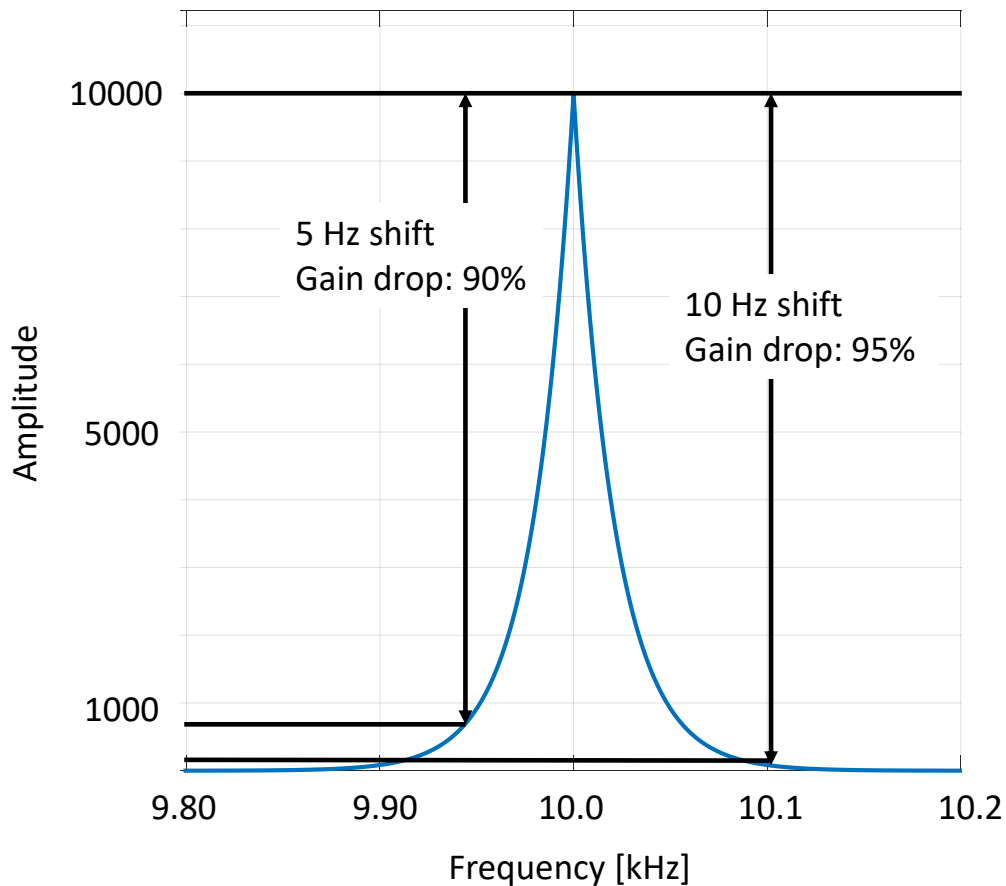


Figure 23. The amplitude provides a higher gain but is more sensitive to frequency variations. Resonant frequency for the sense-mode system is 10 kHz with Q of 10,000. A 5 Hz shift results in 90% gain drop. Adapted from [4].

The theoretical formula for sensitivity ($m/^\circ/s$) was provided by Hou et al. [25]. Sensitivity is defined as the vertical displacement in the sense mode over the angular rate input. The formula is shown below

$$S = \frac{Y_s}{\Omega_z} = \frac{2\omega_x m x_0 / k_{yy}}{\sqrt{\left[1 - \left(\frac{\omega_x}{\omega_y}\right)^2\right]^2 + \left(\frac{\omega_x}{\omega_y Q_y}\right)^2}} \quad (2)$$

where ω_x is the drive mode frequency, ω_y is the sense mode frequency, x_0 is the displacement along the drive direction, Q_y is the Q-factor of the sense mode and k_{yy} is the stiffness coefficient of the sense axis. This analytical model estimates sensitivity as a function of the quality factor, stiffness, and frequency mismatch between the drive and sense modes. From the formula, one can see that, if you decrease the frequency split, the sensitivity increases exponentially. The parameters used to calculate the sensitivity are listed in **Table 3** with their given values.

Table 3. Sensitivity parameters with their given values.

Variable	Value
ω_x	7552.7 Hz
ω_y	7598.9 Hz
x_0	3×10^{-9} m
Q_y	8200
k_{yy}	70 N/m
m	8.76×10^{-8} Kg

The drive and sense mode frequencies (ω_x and ω_y) are obtained from the optimized geometrical COMSOL model. The displacement along the drive direction, x_0 , is obtained from simulation, just as the Q-factor is calculated in simulation. The stiffness coefficient was obtained from Imrul et al. [26]. Generating a larger horizontal displacement with an initial gap results in increased sensitivity.

The sensitivity formula above includes important parameters such as the drive, sense frequencies and the frequency mismatch (split) relating to the sensitivity. Sensitivity can be manipulated by changing drive frequency and the frequency split (difference between drive and sense frequencies), given other parameters such as mass, Q factor, stiffness etcetera remains the same.

Table 4. Sensitivity data with various drive and sense frequencies.

ω_x [kHz]	ω_y [kHz]	Split [Hz]	Sensitivity (m/deg/sec)
7.598	7.598	0	4.62e-10
7.552	7.598	46	4.69e-12
17.5	7.598	9902	3.05e-14
17.5	14.5	3000	2.874e-13

$$S_{_2} = \frac{Y_s}{\Omega_z} = \frac{2(7552)(8.76e-8)(3e-9)/70}{\sqrt{[1 - (\frac{7552}{7598})^2]^2 + (\frac{7552}{7598 * 8200})^2}} = 4.69e-12$$

$$S_{_3} = \frac{Y_s}{\Omega_z} = \frac{2(17500)(8.76e-8)(3e-9)/70}{\sqrt{[1 - (\frac{17500}{7598})^2]^2 + (\frac{17500}{7598 * 8200})^2}} = 3.05e-14$$

Figure 24. Sample calculations for two drive and sense frequencies illustrating a higher sensitivity with $S_{_2}$ having lower split.

Table 4 illustrates different sensitivity values for different pair of drive and sense frequencies, showing the change in sensitivity with change in drive frequency as well as change in split. Sensitivity is maximized when the frequency split is zero (first row in **Table 4**) and is lowest (3rd row in **Table 4**) when the split is the greatest. Also, if we keep the sense frequency constant and increase the drive frequency to higher resonance for example to another mode at 17.5 kHz, the sensitivity decreases as seen in row 3 in **Table 4**. This is because increasing ω_x will increase the numerator in equation (2) but it also increases the denominator. The rate of increase of the

denominator is higher compared to the rate of increase in the numerator thus decreasing the sensitivity. To describe this mathematically, **Figure 24** shows two sample calculations of sensitivity for a case when just the drive frequency is increased to higher value, for $\omega_x = 7.598$ kHz and $\omega_x = 17.5$ kHz when ω_y is constant which results in a sensitivity of 4.69×10^{-12} and 3.05×10^{-14} $m/^\circ/s$ respectively. When the value of ω_x is increased, the sensitivity decreased by orders of magnitude because frequency split also increases. This analysis shows the dominating parameter in the equation is the split. Increasing ω_x only will decrease the sensitivity. Sensitivity can be improved by decreasing the split.

If one was to increase the Q-factor the sensitivity would increase to a certain point and then stop, as it is dependent on other factors. A Q_y of 10 will decrease the sensitivity to 7.26×10^{-10} ($m/^\circ/s$) while Q_y of 10,000 will result in to 3.69×10^{-9} ($m/^\circ/s$). The Q factor can be increased by vacuum packaging. The stiffness coefficient, k_{yy} , will produce a higher sensitivity if it has a lower value, as this results in the device being less rigid, making it easier to vibrate at its natural frequency for longer period of time. If the k_{yy} value is reduced to 10, the sensitivity is increased to 2.59×10^{-8} ($m/^\circ/s$). If the k_{yy} value is increased to 500, this results in a decreased sensitivity of 5.17×10^{-10} ($m/^\circ/s$). The mass m of the gyroscope structure can also affect its performance. Maximizing the mass that generates the Coriolis force while minimizing the total mass excited by the Coriolis force will increase the sensitivity [4]. If the mass is increased from 1.16×10^{-8} to 1.1600×10^{-3} kg, the sensitivity is increased to 3.694×10^{-5} ($m/^\circ/s$). If the mass is decreased further to 1.16×10^{-12} kg, then the sensitivity is reduced to 3.694×10^{-14} ($m/^\circ/s$).

The analysis was carried out in MATLAB and **Figure 25** illustrates a sensitivity of 10^{-12} ($m/^\circ/s$) with a frequency split of 10 Hz.

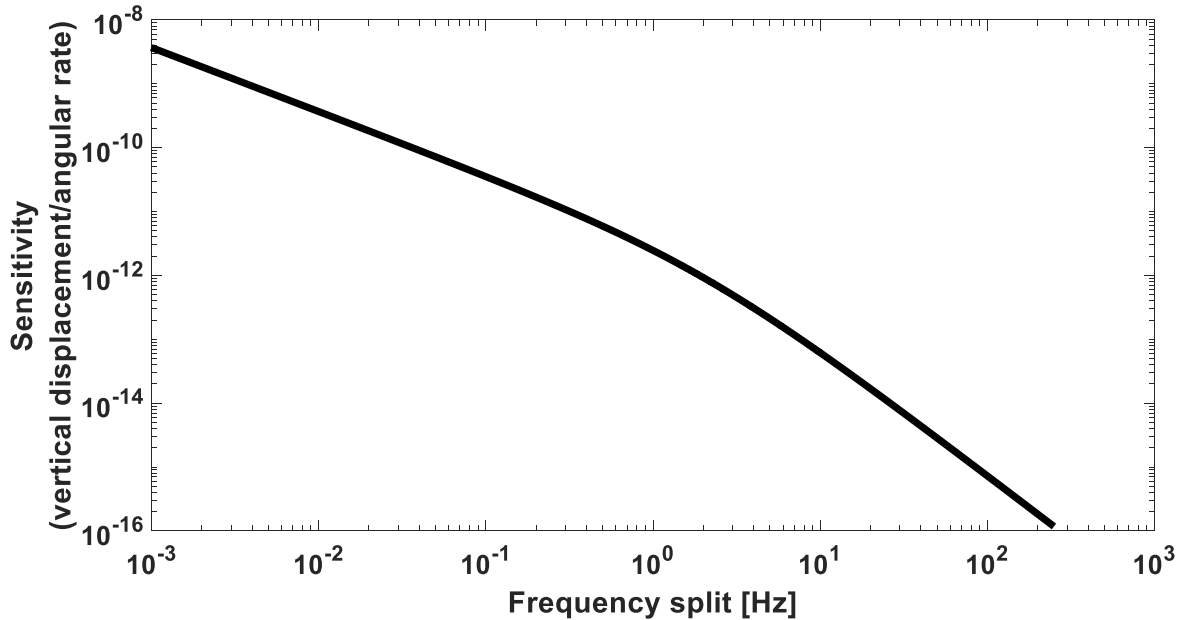


Figure 25. Sensitivity decreases with an increase in frequency split. Sensitivity is the ratio between vertical displacement and the rate of rotation.

Comb Drive Actuation

The butterfly proof masses will be actuated using electrostatic force via comb drive. The four proof masses have a comb drive design on one side, while the opposite side connects to the paddle beam. This is the device's electrostatic force actuator. Comb drives are used in sensing technologies for rotational and translational motion. The comb drive on the butterfly gyro uses two conductive electrodes at different potentials. The proof mass itself is set to a floating potential and the bottom electrodes have a bias voltage applied to them. The proof mass design is similar to a parallel plate with a comb drive attached to its end, as shown in **Figure 26**.

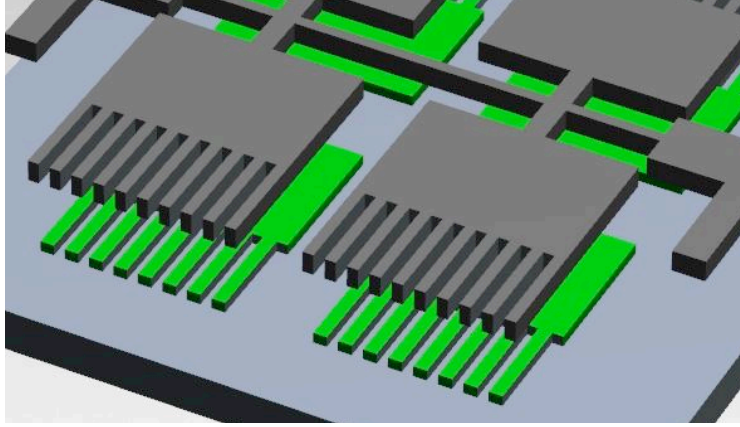


Figure 26. Cut-out view of proof mass in grey and electrodes in green. The proof mass has a floating potential node while the electrodes have bias voltage applied to them.

The comb drives provide motion in the same plane and are used to drive the gyroscope. The parallel plate can provide out-of-plane motion with the external angular rate input. The gyroscope structure uses a push-pull driving scheme. The capacitance of a parallel plate actuator is

$$C(x) = \frac{A\epsilon\epsilon_0}{x} \quad (3)$$

where A is the area of overlapping electrode, x is the distance between two plates, ϵ_0 ($=8.854 \times 10^{-12}$ F/m) is the permittivity of free space and ϵ is the relative permittivity of air, which is approximately equal to one. Using the energy of the capacitor-battery system, the normal force applied to the movable plate of the capacitor is (4) where V is the voltage applied and the negative sign indicates the force is attractive [27]. The tangential force then becomes (5) where b is the width of the plate and d is the distance between the plates. The tangential force pulls the movable plate for more area.

$$F_N = -\frac{A\epsilon\epsilon_0}{2x^2} V^2 \quad (4)$$

$$F_T = \frac{b\epsilon\epsilon_0}{2d} V^2 \quad (5)$$

To drive the mechanical structure into resonance, a DC bias voltage with an AC signal is applied across the electrodes (there is no DC current associated with the DC bias). The push-pull driving scheme is used on the comb resonator with the following voltages [27]:

$$\begin{aligned} V_1 &= V_{dc} + V_{ac} \sin \omega_d t \\ V_2 &= V_{dc} - V_{ac} \sin \omega_d t \end{aligned} \quad (6)$$

Substituting (6) into (5) results in (7). Using these relationships to simplify the equation yields (8).

$$F_d = \frac{b\epsilon\epsilon_0}{2d} (V_1^2 - V_2^2) \quad (7)$$

$$F_d = \frac{2bn\epsilon\epsilon_0}{d} (V_{dc}V_{ac} \sin \omega_d t) \quad (8)$$

The driving force variables include b , which is the length of the comb, n is the number of fingers in the comb structure and d is the lateral distance between movable electrodes and fixed electrodes.

The normal force then becomes (9) where A is the area of overlapping comb teeth.

$$F_N = -\frac{A\epsilon\epsilon_0}{2d^2} (V_1^2 + V_2^2) \quad (9)$$

Simplifying the equation using (6) results in (10).

$$F_N = -\frac{A\epsilon\epsilon_0}{d^2} (V_{dc}^2 + V_{ac}^2 \sin^2 \omega_d t) \quad (10)$$

The horizontal driving force is related to the length and number of comb teeth. To obtain a greater driving force, one can increase the comb length and reduce the lateral distance between the structural layer and the electrode underneath (**Figure 27**). The driving force is also increased by increasing the number of electrodes in the array (**Figure 28**). From the analysis, the gap between the fixed electrode and the movable proof mass can significantly affect the drive force. The fabrication process limits the gap, so the selected gap is three μm . The number of electrodes was 10, as this provided the maximum drive force with a good detection area.

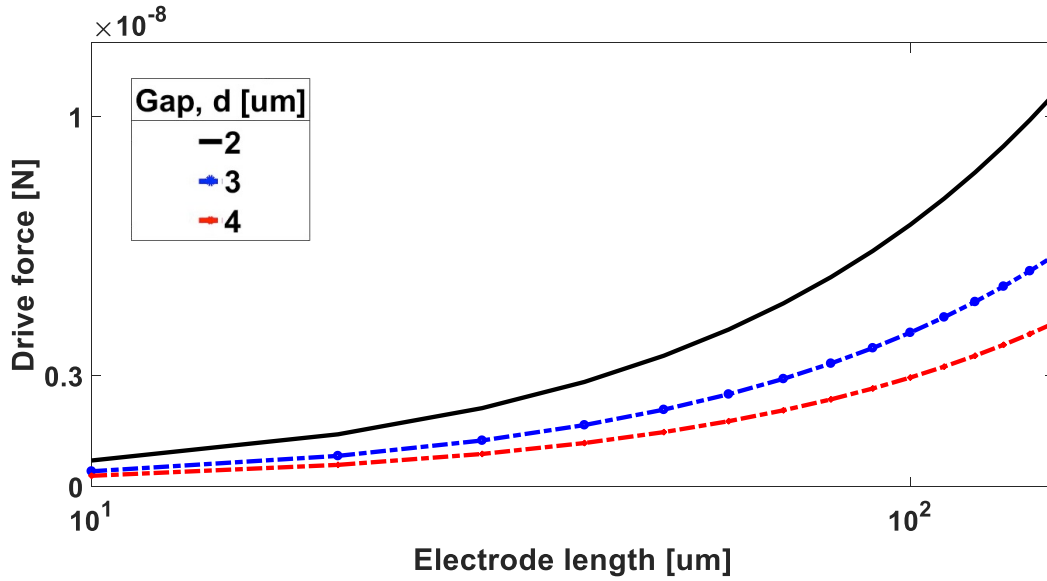


Figure 27. Drive force vs electrode length showing an increase in electrostatic force as lateral distance (d) decreases.

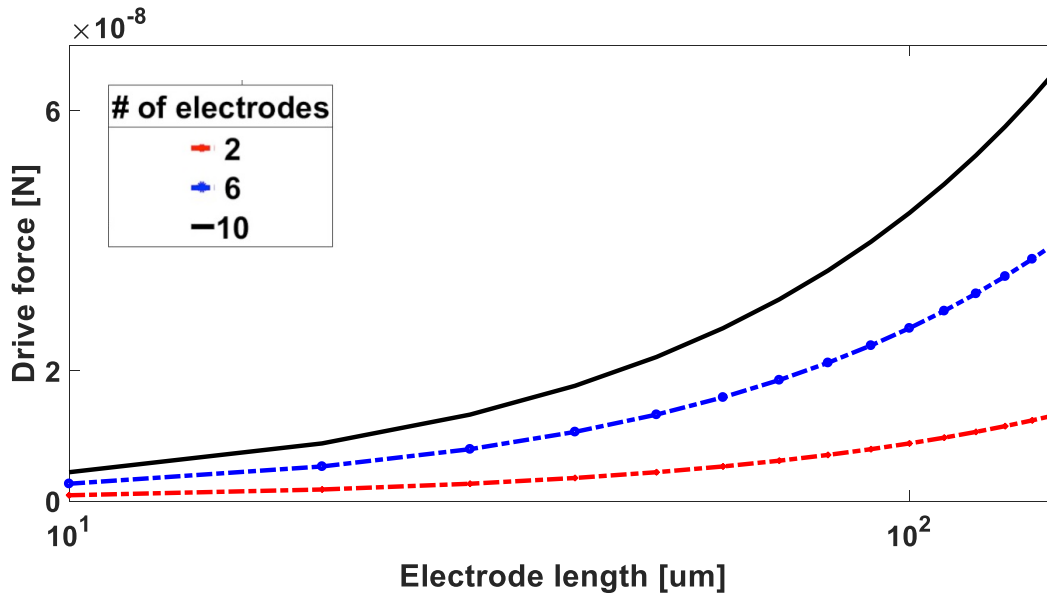


Figure 28. Drive force vs electrode length showing an increase in drive force as the number of electrodes in the array are increased.

The parameters used to calculate the tangential and normal forces are listed in **Table 5**.

Table 5. Drive and sense force parameters with their given values.

Parameter	Value
A	$3.3 \times 10^{-8} \text{ m}^2$
ϵ_0	$8.854 \times 10^{-12} \text{ F/m}$
ϵ	1
d	$3 \times 10^{-6} \text{ m}$
V_{dc}	5 V
V_{ac}	0.1 V
b	$150 \times 10^{-6} \text{ m}$
n	10

A tangential and normal electrostatic force of 4.3 nN and 811 nN, respectively, are observed with the given parameters.

Stationary Analysis

Stationary analysis was performed to understand the correct drive and sense modes during electrical actuation. The stationary analysis consists of the electrostatic model for the butterfly structure, electrodes, and an air domain shown in **Figure 29**. This model uses the frequency model but with the added components. This study is performed to ensure the correct mode shape during operation. The study solves the structural mechanics with applied DC bias problem. Symmetric and antisymmetric vibrational modes are computed, which correspond to specific resonant peaks in the presence of an electric field. The electrodes, which are used to drive the gyroscope, sit on top of the silicon nitride (shown in purple) and underneath the four proof masses.

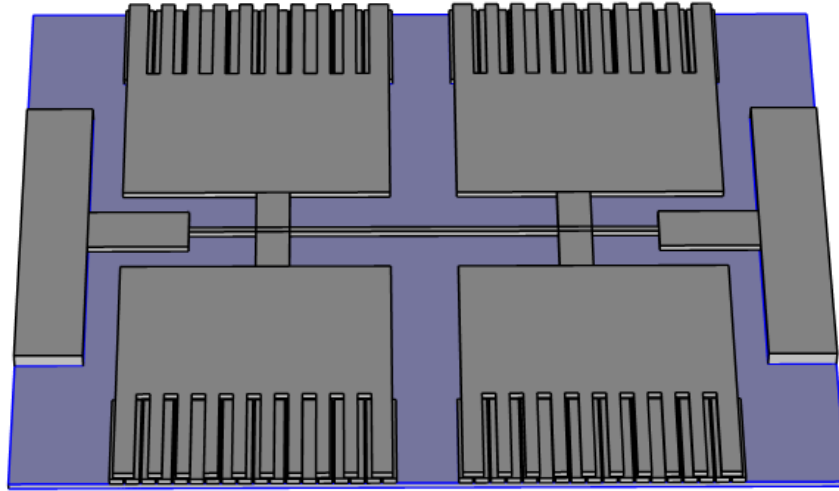


Figure 29. *Electrostatic actuation and sensing model of butterfly gyroscope. This includes the nitride layer (in purple), fixed electrodes, butterfly resonator and air domain (not shown).*

There is a gap of three μm between the proof masses and the electrodes. This is the air gap where the capacitance builds up. The silicon nitride acts as an isolation layer between the structure and the wafer. This layer is used to electrically isolate the MEMS device from the silicon substrate. The electrodes consist of 10 fingers with a length, width and depth of 150 μm , 20 μm and 10 μm , respectively. The entire model is enclosed by an air domain that acts as a medium for the electrostatic forces. A fixed constraint is applied at the base of the anchor and drive electrodes, as highlighted in **Figure 30**.

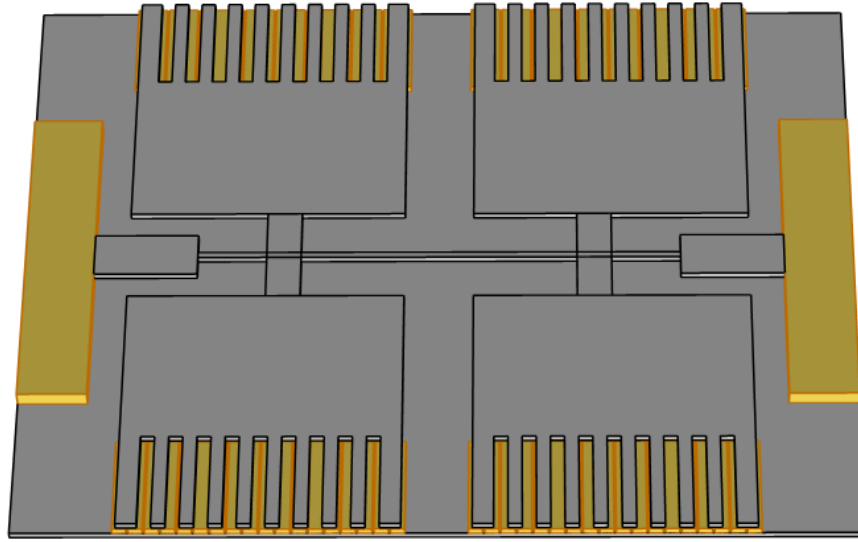


Figure 30. Butterfly gyro model with highlighted electrodes and anchors as fixed constraint.

In operation, an input drive voltage consisting of a DC bias potential with an AC component is applied across the drive electrodes in an alternating manner, as shown in **Figure 31**.

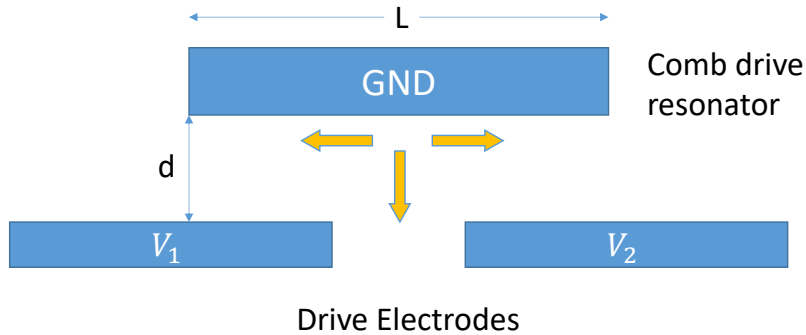
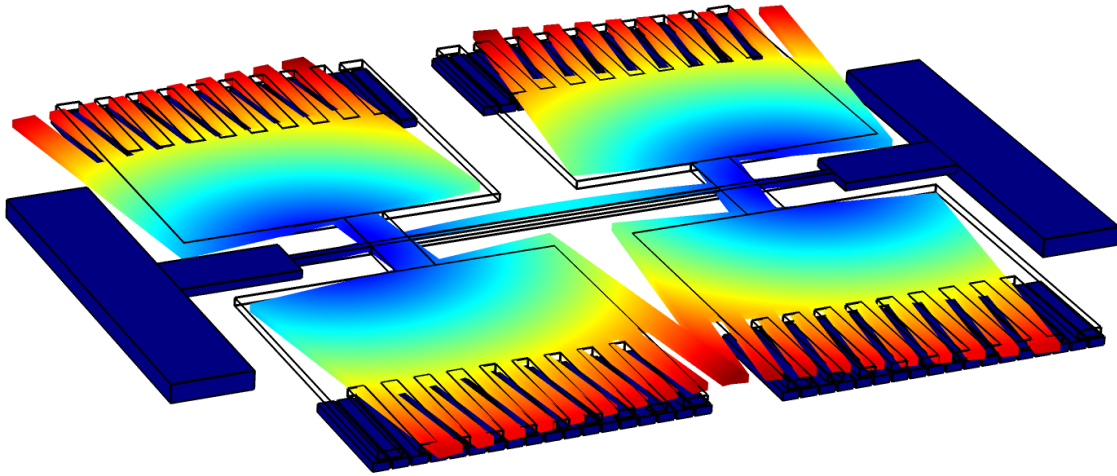


Figure 31. Schematic of voltages applied to the electrodes underneath the proof mass. The drive electrodes include a DC bias potential that oscillates the proof mass into resonance.

The voltages V_1 and V_2 take on the form shown in equation (6). The underlying silicon nitride is grounded and the silicon resonator acts as a floating potential. A DC bias voltage up to 20 volts is applied. The assumption has been made that the silicon must be heavily doped to be considered a perfect conductor, so the bias voltage is applied using the domain terminal feature. The electrical field is assumed to be zero inside the resonator, so there are no volumetric electrical forces.

a)



b)

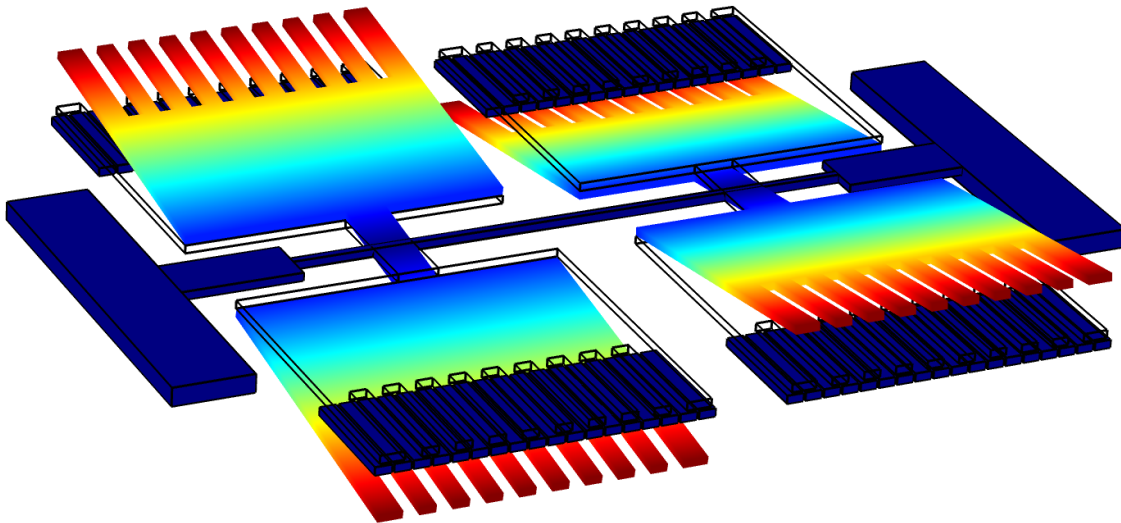


Figure 32. Electric potential surface plot showing (a) drive mode gyro displacement and (b) corresponding orthogonal sense mode displacement.

Figure 32 shows the electric potential surface plots for both the drive and sense modes of operation. Voltages V_1 and V_2 have been applied to the electrodes at the bottom in an alternating manner. As one can see, this displacement in the drive and sense modes is identical to the natural frequency mode shapes shown in Figure 12 and Figure 13. The red illustrates the maximum displacement,

which is on the edge of the proof masses, and shades of blue represent little-to-no displacement. The drive electrodes are present where there is maximal displacement. **Figure 33** illustrates the vertical displacement of sensitivity as a function of applied bias, which takes on the form shown in (6). As the electric potential increases on the drive electrodes, the sensitivity increases. At its maximum point, a value of 26 nm is observed.

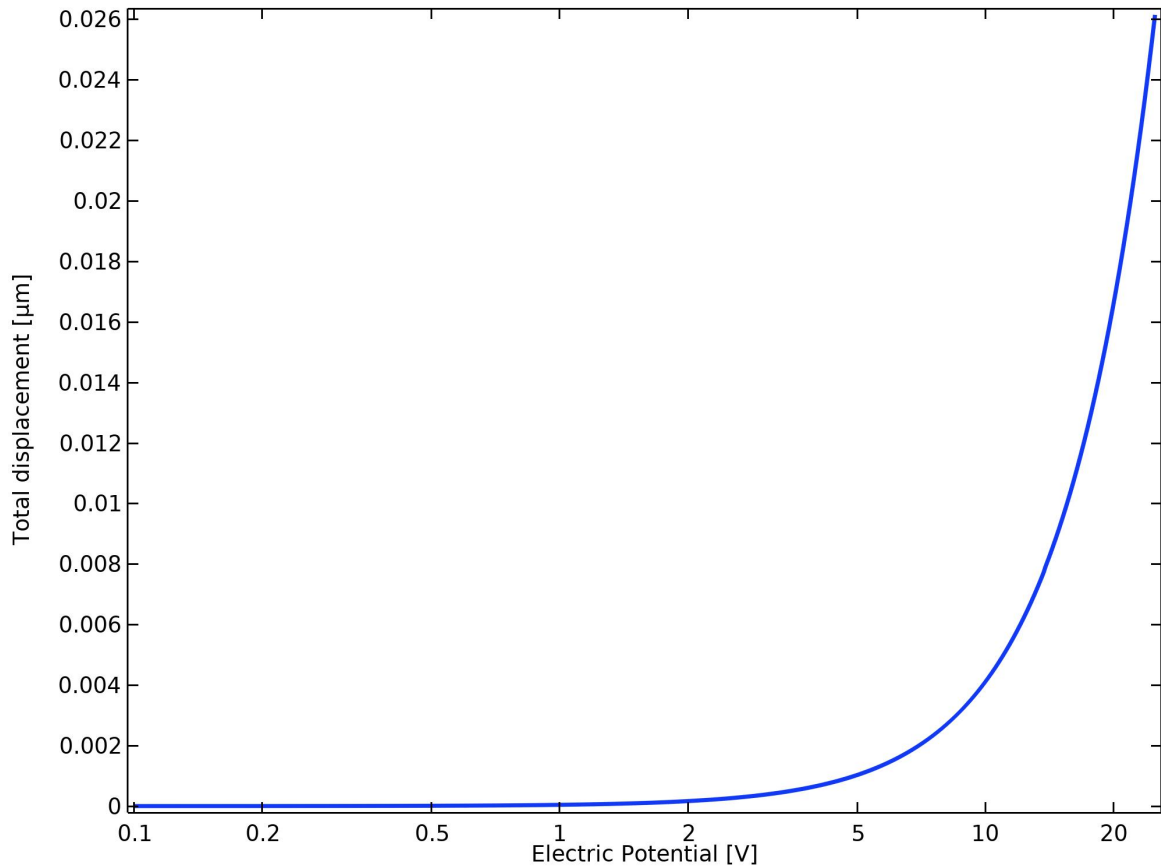


Figure 33. Displacement in the sense axis as a function of electric potential with a maximum of 26 nm.

The disadvantages of this design include limitations due to the electrode gap. There is an initial gap between the structure and the electrodes. When the butterfly gyro is in its drive mode, it is oscillating in the same plane horizontally and in its sense mode, it is oscillating out of plane vertically. The sense mode is limited by the gap which is determined by the fabrication design rules.

The proof mass is used as a movable electrode and the fixed electrode is under the proof mass, with an initial gap distance of d . The proof mass is labeled as GND and the fixed electrodes as V_1 and V_2 , as shown in **Figure 31**. When the electrodes are supplied with a voltage difference V_1 and V_2 , an electrostatic force is applied to the mass, which pulls it towards the fixed electrodes. As you increase the bias voltage, the proof mass is displaced further. An elastic restoring force by the paddle beam pulls the proof mass back towards its original position. Problems arise due to the nonlinear nature of the electrostatic force which can cause instability in certain conditions. When the motion of the proof mass is too great, the moving proof mass can stick onto the fixed electrodes, which is known as the pull-in effect. This is an electrostatic phenomenon where the conductive electrodes snap onto each other at certain voltages and can damage the device. This happens at approximately one-third of the initial gap distance [27], [28]. Research has been done in order to address this issue, but achieving a large displacement requires a complex design and process [29]. The pull-in voltage is the point when the electrostatic force and the mechanical recovery force are balanced, and this was calculated using two different formulas. If one keeps increasing the bias voltage, the mechanical force will continue to grow linearly, while the electrostatic force will grow nonlinearly. This will cause the two electrodes to be pulled against each other until they make contact. If the electrodes are in contact, they can only be released when the bias voltage is taken away completely (i.e. $V=0$). The pull-in voltage is defined by Bao, Minhang [27] as

$$V_{p1} = \sqrt{\frac{8kd^3}{27A\epsilon\epsilon_0}} \quad (11)$$

where k is the spring force constant, d the original gap distance, A the overlapping area of the electrodes, ϵ the relative permittivity of the medium between two electrodes, and ϵ_0 the

permittivity of vacuum. Another variation of the formula was used to verify the pull-in voltage given by Liu, Chang [28] and is

$$V_{p2} = \frac{2x_0}{3} \sqrt{\frac{k}{1.5C_0}} \quad (12)$$

where x_0 is the original gap distance, k the spring force constant and C_0 the capacitance between two electrodes. In (11), if one changes the relative permittivity of the medium ϵ , the pull-in voltage will decrease significantly at first and then start to slow down. The area can also affect the pull-in voltage. If the overlapping area A is increased, the pull-in voltage will start to decrease in magnitude. In (12), one can decrease the original gap distance x_0 to increase the overall capacitance. This is illustrated in **Figure 34**, where the electrode gap is varied from 1 to 10 μm and, as you decrease the gap, the capacitance increases. This, however, will reduce the pull-in voltage drastically. To increase the pull-in voltage, one can increase the spring stiffness k , which results in a more rigid structure.

The values used to calculate the pull-in voltage are listed in **Table 6**. A pull-in voltage of 21.89 volts was found with the values given below for both V_{p1} and V_{p2} .

Table 6. Parameter values used to calculate pull-in voltage.

Variable	Value
k	70 N/m
d	3 μm
A	$1.32 \times 10^{-7} \text{ m}^2$
ϵ	1
ϵ_0	$8.854 \times 10^{-12} \text{ F/m}$
C_0	$3.89 \times 10^{-13} \text{ F}$

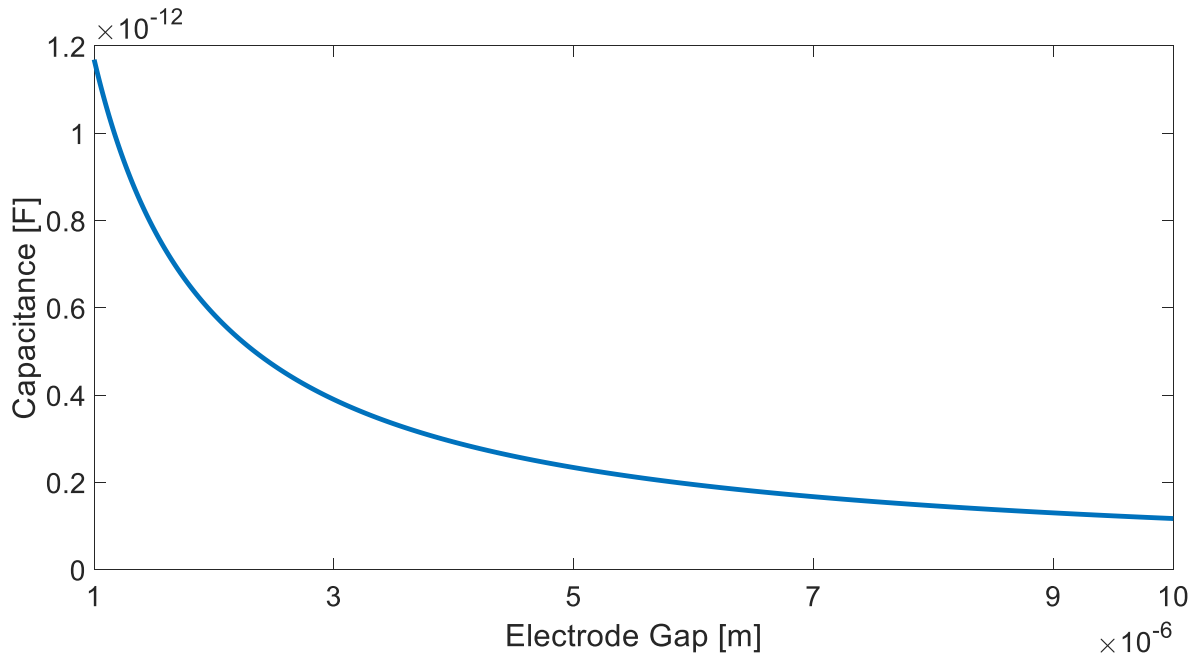


Figure 34. Capacitance as a function of electrode gap showing an increase as the gap is reduced from 10 to 1 μm .

Damping

In MEMS vibratory gyroscope the resonant mass needs to be continuously oscillating if possible, without pumping energy. Various damping acting on the mass will stop the vibration that are related to different energy loss mechanisms. Different types of damping exist in the butterfly gyro. These energy dissipation mechanisms include anchor loss, surface loss, internal dissipation and thermoelastic dissipation (TED). As the proof mass oscillates in the drive and sense modes of operation, part of the vibrational energy is dissipated to the anchor due to wave radiation. This phenomenon is called anchor loss [30]. In order to reduce anchor loss from the wave propagation, the resonator should be designed to place the anchor at the nodal points of the wave, where the mode displacement is zero [30]. Surface loss arises from energy dissipation through defects, impurities and roughness. Surface loss becomes important when the resonator size is small due to the increased surface-to-volume ratio. This dissipation mechanism can be reduced by surface

treatments such as annealing [31]. Internal dissipation in a resonator occurs from internal friction due to the motion of crystallographic defects [32]. One can use a high-quality single crystal material to minimize internal friction. Thermoelastic dissipation occurs when the resonator is vibrating and some parts of the resonator experiences tension while others experience compression. These stresses and strains produce a local temperature gradient on the resonator's surface from the hot and cold regions. As the resonator relaxes back to its thermal equilibrium, heat flows irreversibly from hot to cold regions [30]. This results in entropy generation and energy dissipation [32].

Quality factor (Q) is a non-dimensional parameter that is used to evaluate the performance of a resonator. Q factor is defined as the ratio of the average stored energy to energy dissipated per oscillation period. It tells how underdamped a resonator is and defines a resonator's bandwidth relative to its center frequency. A higher Q indicates a lower rate of energy loss, so the oscillation lasts for a longer period. Navigation-grade gyroscopes have a high Q factor with low damping, so they can vibrate much longer compared to a commercial grade sensor.

To characterize the MEMS device, the Q factor is evaluated using finite element method software.

For 3-D structures, the Q can be found using the following equation:

$$Q = \frac{1}{2} \left| \frac{Re(\omega)}{Im(\omega)} \right| \quad (13)$$

where $Re(\omega)$ and $Im(\omega)$ are the real and imaginary parts, respectively, of the angular resonant frequency of that mode [33]. COMSOL Multiphysics 5.3a is used to solve this thermo-mechanical eigenvalue problem numerically. A biased eigenfrequency study was used to calculate the resonant frequency. For the drive and sense modes of operation, frequencies of $8271.7 + 0.50257i$ Hz and

8047.3 + 0.49239i Hz were observed, respectively. The imaginary part of the frequency corresponds to the rate of energy loss in the system. This equates to a Q factor of 8,229 and 8,172 for the drive and sense modes, respectively.

Viscous air damping exists in resonators when they shift from vacuum to atmospheric pressure. This damping increases rapidly as the resonator's surface-to-volume ratio decreases [34]. The Q factor due to air pressure alone was given by Newell, W. [34] and is

$$Q = (\pi/2)^{1.5} \rho d f [(RT/M)^{0.5} / (1/P)] \quad (14)$$

where ρ is density in kg/m^3 , d the thickness in m , f the resonant frequency in Hz , R the universal gas constant in joules per degree Kelvin, T the temperature in Kelvin, M the molecular mass of air in kg and P the pressure in N/m^2 . This formula assumes individual air molecules exchange momentum with the resonator "at a rate proportional to the difference in velocity between the air molecules and the resonator" [34]. The parameter values used to calculate the Q factor are listed in **Table 7**. A Q factor of 1.66×10^4 is observed with the given values for the designed resonator.

Table 7. Parameter values used to calculate Q due to air pressure.

Parameter	Value
ρ	2329 kg/m^3
d	$10 \times 10^{-6} m$
f	7552.7 Hz
R	8317 $J/^\circ K$
T	293.15 K
M	$28.97 \times 10^{-3} Kg$
P	1 Pa

Figure 35 shows the results of (14) for the butterfly gyro. The pressure is varied from 0 to 1 Pa. The graph illustrates that, as the air pressure is reduced to a vacuum, the Q factor increases significantly. The Q factor is not the total Q , as it does not consider other damping mechanisms, such as TED and anchor loss.

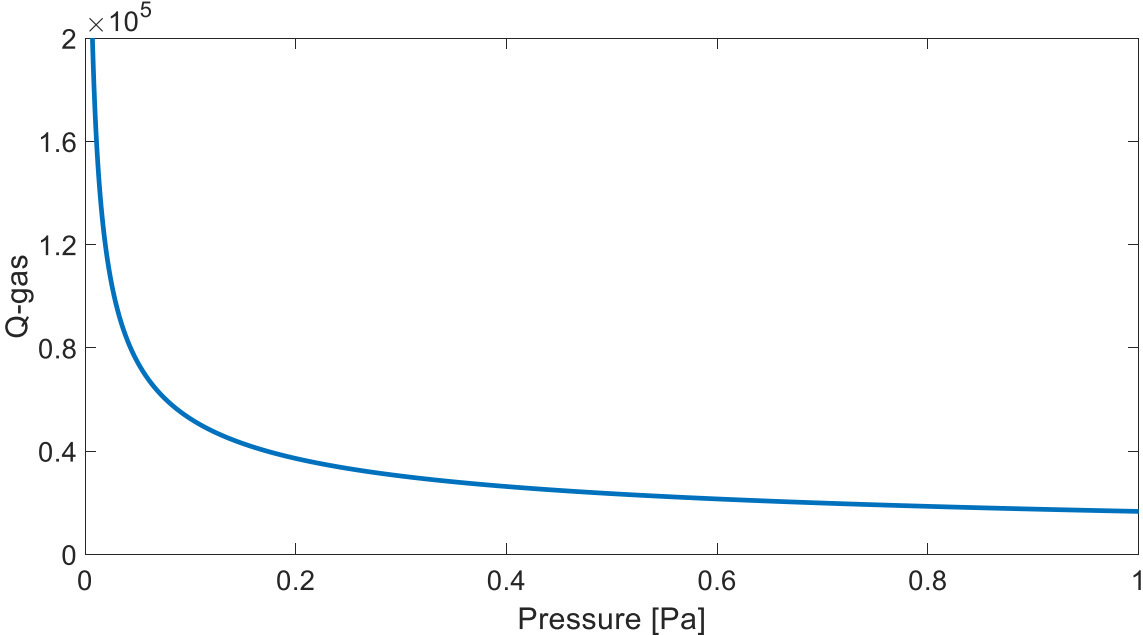


Figure 35. Pressure vs Quality factor for the butterfly gyro, illustrating an increase in Q as the pressure decreases.

Frequency Response

A frequency domain analysis was performed on the gyroscope model to understand the amplitude responses at the resonance frequencies and to identify energy losses. This involved the application of a drive voltage of 5 V DC offset with an addition of 100 mV as harmonic perturbation. A fine mesh with physics-controlled setting is used to achieve the frequency response graph shown in **Figure 36**.

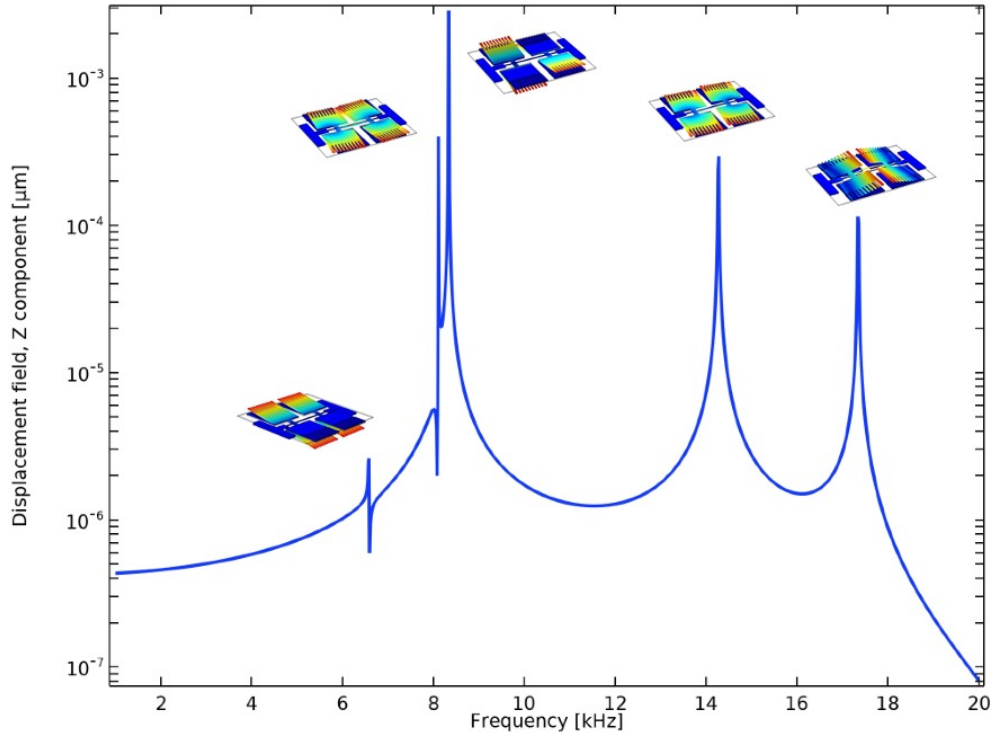


Figure 36. Frequency response from the simulated model showing multiple peaks under linear drive conditions. The ones of interest are located around 8 kHz with maximum amplitude corresponding to sense mode.

The frequency was swept from 1 kHz to 20 kHz and the response was graphed. The y-axis is the displacement field with the z component. At different frequencies, the mode shape is recorded and a snapshot is included with the curve. As one can see, the drive and sense modes are close to 8 kHz with the sense mode having the maximum amplitude. There are other mode shapes, but they are distorted, so implementing them would create a sizable challenge. The distorted mode shapes are also significantly apart from each other, so the sensitivity would decrease. A zoomed-in view of the frequency characteristic is shown in **Figure 37**, illustrating the drive and sense mode frequencies from the optimized model. The predicted drive and sense frequencies are 8.11 and 8.33 kHz, respectively.

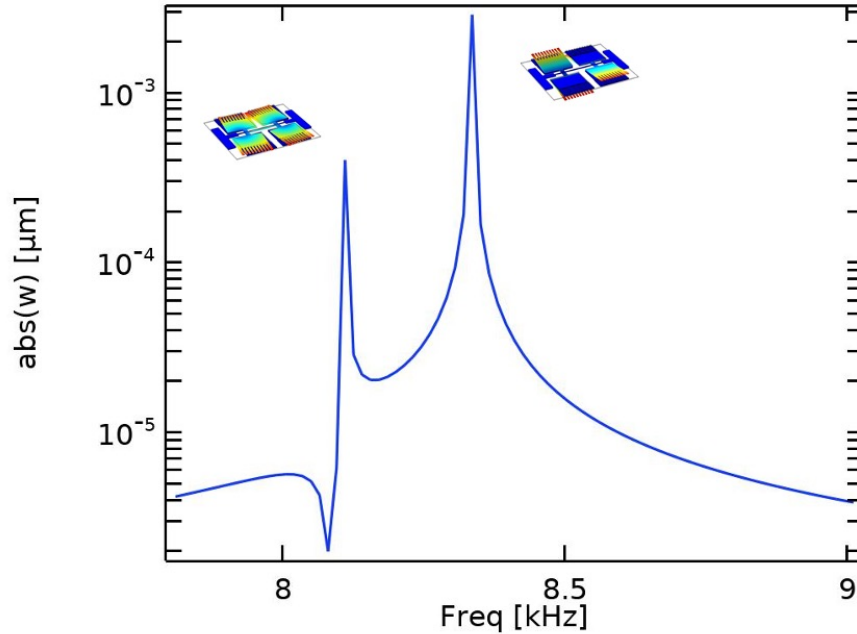


Figure 37. Zoomed view of the drive and sense mode operating frequencies at 8.11 and 8.33 kHz, respectively.

Reducing the drive and sense frequency mismatch is important, as this aids in enhancing the sensitivity of the gyroscope. The two modes of operation affect the rate of rotation within the sensitivity formula given in (2). A reduction in frequency mismatch improves the sensitivity drastically. A greater drive and sense frequency does not necessarily translate into improved sensitivity. It is the frequency mismatch that dictates the spectrum. The electric potential is related to the sensitivity, as it directly affects the vertical displacement. As the gyroscope is driven into resonance by the horizontal electrostatic forces, an input angular rate causes the Coriolis force to displace the gyro. The amount the gyro displaces depends on the drive forces. As shown in **Figure 33**, a greater applied potential generates a larger vertical displacement. The voltage can be increased to a certain point, but increasing beyond that would cause the modes shapes to be distorted, resulting in the pull-in effect. The drive mode oscillation is an important parameter as it relates to the displacement of the gyro. It includes a sinusoidal drive mode excitation force given in (8). The phase and the frequency of the drive oscillation directly determine the sense mode

response [27]. This is related to the sensitivity by the vertical displacement Y_s , where x_0 dictates the displacement along the drive direction. A greater driving force induces a greater Coriolis force, which in turn improves the sensitivity of the gyro.

Chapter 3

Prototype Fabrication

After the butterfly gyroscope design was defined and modeled, it was then tuned through structural optimization, which reduced the frequency split between the drive and sense modes. This resulted in an enhanced sensitivity with a maximized Quality factor. After this, fabrication platforms were explored. To this end, one fabrication approach was most appealing: the PolyMUMPS, a commercially available fabrication process that allows out of plane actuation and sensing suitable for this design as outlined in previous chapters. This is a commercially available process, flexible, versatile and it allowed the placement of out-of-plane electrodes at the bottom of the suspended proof mass.

Therefore, butterfly gyro was fabricated using PolyMUMPS (poly-crystalline silicon multi-user MEMS process) [35]. This is a three-layer polysilicon surface micromachining process. One must follow the design rules and adhere to its tolerances for a successful fabrication. This includes complying with the thickness of each layer, spacing between layers and overall size of its geometry. One can change the shape of the layers and length of the components being fabricated.

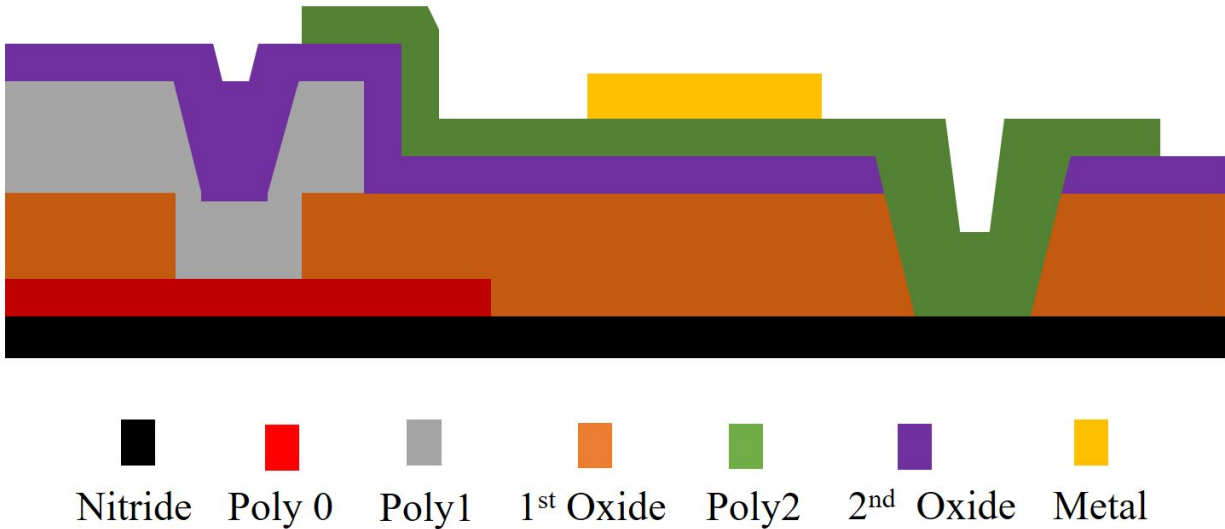


Figure 38. Cross sectional view depicting the 7 layers of the PolyMUMPS process. Adapted from [35].

Figure 38 is a cross section view of the three-layer polysilicon PolyMUMPS process [35]. This process has the standard surface micromachining features. The first layer is silicon nitride which is used as a hard mask. It protects the silicon from etching and is used to electrically isolate the MEMS device from the silicon substrate. The second layer is the poly0 layer which is the first polysilicon mechanical layer. This layer does not move, acting as an electrical ground plane. One can apply different voltages to this layer for actuation purposes. Not using this layer will result in the MEMS device sticking to the nitride layer. The third layer is the first oxide. This layer dictates the amount of gap you will have between the two poly layers (poly0 and poly1). This layer is a sacrificial layer that will be released at the end of the process. The fourth layer is the poly1 layer, which is the second mechanical layer. This is where the mobile parts of the MEMS device will be shaped. On top of this layer lies the second oxide, which is the fifth layer. This layer works similarly to the first oxide, except with a different thickness. The sixth layer is the poly2, which is the third mechanical layer. This layer is similar to the poly1 layer but with a different thickness. The final layer in the topology is the metal layer. This is used for probing, bonding and electrical routing connections to the bond pads [35].

PolyMUMPS Process

This surface micromachining process is designed to be as general as possible to support different designs on a single wafer [35]. The process starts with 150 mm n-type silicon wafers of 1-2 ohm-cm resistivity [35]. The surface is heavily doped with phosphorus in a diffusion furnace, which helps prevent charge feedthrough from the electrostatic devices on the surface. Next, a low-stress LPCVD (low pressure chemical vapor deposition) silicon nitride is deposited on the wafer. This is followed by the deposition of a 500 nm LPCVD of the poly0 layer, which is patterned by photolithography [35]. On top of the poly0, photoresist is spun on and then patterned, as shown in

Figure 39a.

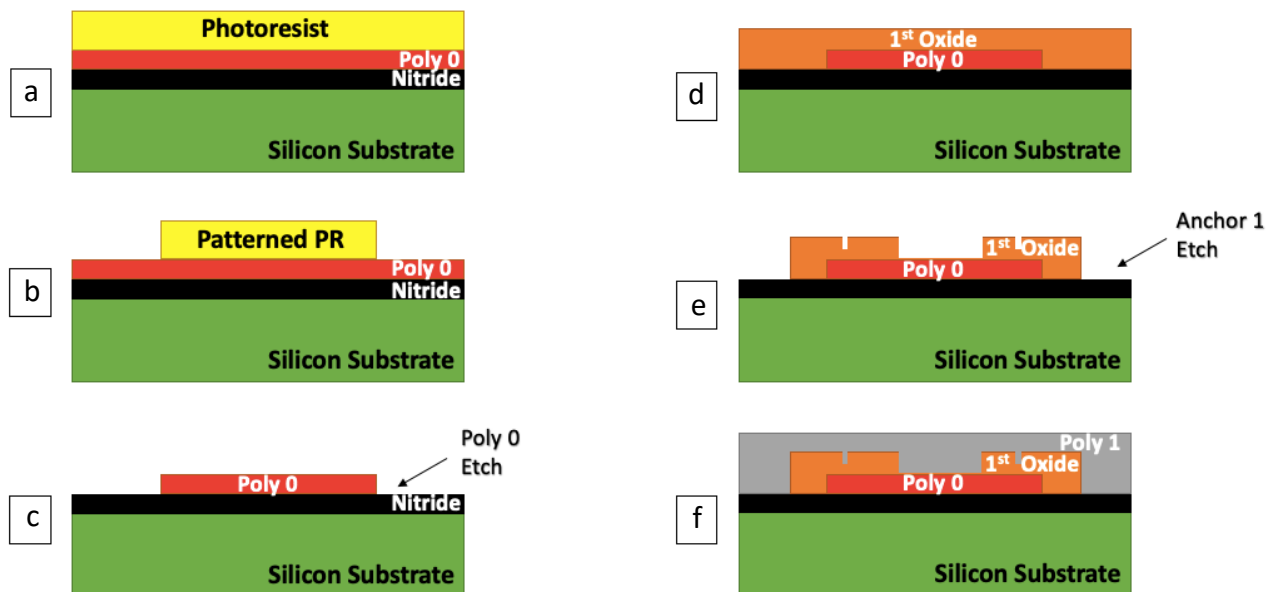


Figure 39. Cross-sections depicting the PolyMUMPS fabrication process steps for the proposed butterfly gyro.

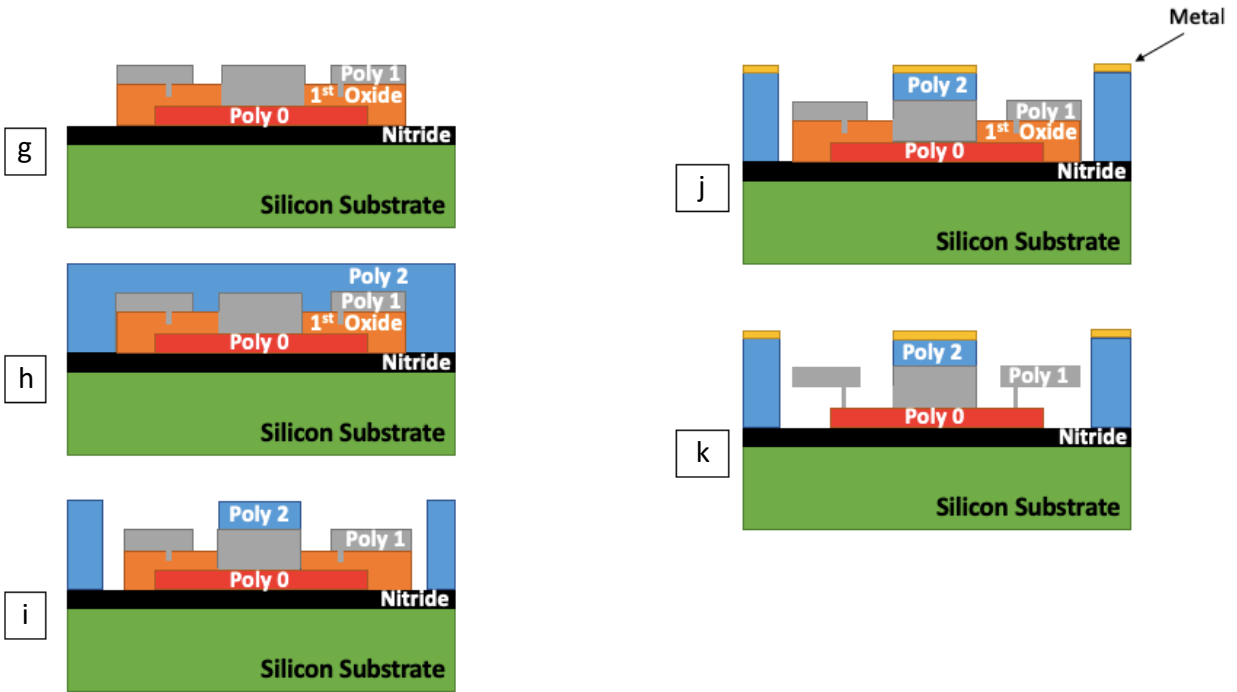


Figure 40. Cross-sections depicting PolyMUMPS fabrication process steps for the proposed butterfly gyro (cont.).

A silicon mask sits on top of the photoresist and ultraviolet light (UV) is shined through the exposed parts, as shown in **Figure 41**. The mask has direct contact with the photoresist and the UV light will image the wafer. In the places the mask is clear, UV light will pass through to the exposed photoresist and, in the areas the mask is dark, the photoresist will not be exposed. This is known as positive resist, where the mask is directly transferred.

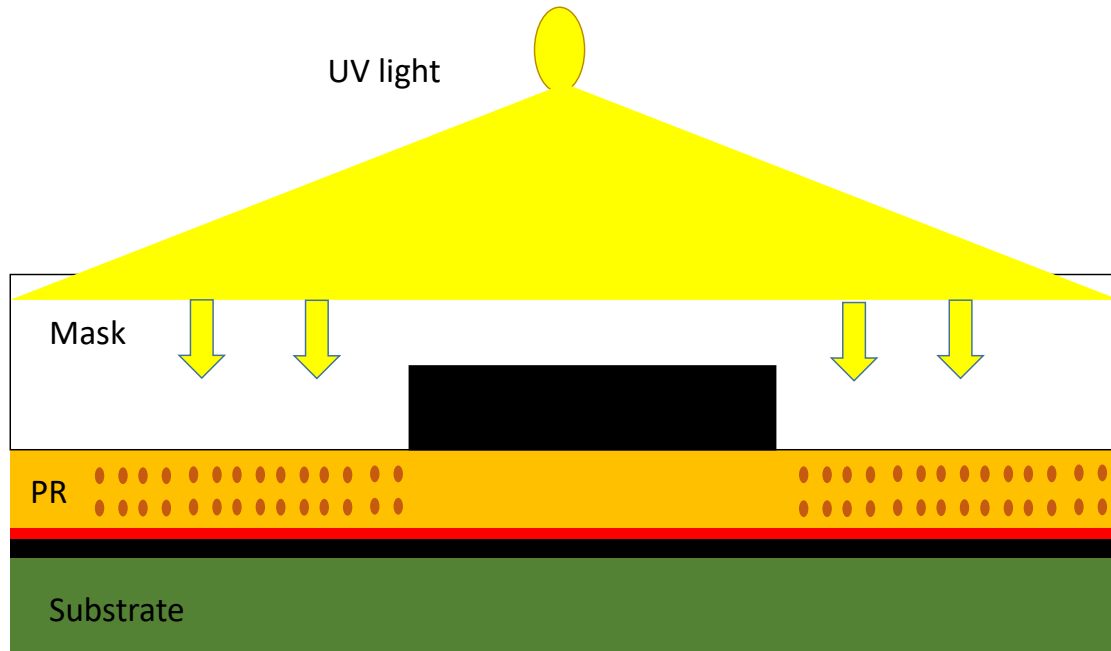


Figure 41. Photolithography process during exposure of photoresist using a positive tone, where exposed areas are being removed to etch the underlying structural layers.

After the photoresist has been exposed, it becomes acidic and is put in a solution of acids and bases, which removes the exposed photoresist (**Figure 39b**). After patterning the photoresist, the wafer etches parts of the poly0 layer, which is not coated with the photoresist (**Figure 39c**). This is done using the reactive ion etching process (RIE). Then, the photoresist is removed in a solvent bath. Using photolithography, one can take the pattern from the mask, transfer it to the photoresist and finally pattern the poly0 layer. The next step is to deposit the first oxide layer of 2.0 μm by LPCVD, which will be removed at the end of the process (**Figure 39d**). This oxide layer is lithographically patterned with dimples using a dimple mask in a RIE system (**Figure 39e**) [35]. This is done to avoid stiction, which arises when two flat materials are very close to each other and are almost touching. They can potentially get stuck to each other, as intermolecular forces and van der Waals forces are very strong over short distances. Then the oxide is patterned with an anchor1 mask and then reactive ion etched. After etching, the first structural layer of polysilicon (poly1) is deposited at a thickness of 2.0 μm (**Figure 39f**) [35]. This layer is doped to convert it

from a semiconductor to a conductor using phosphorus. Then, a layer of phosphosilicate glass (PSG) is deposited over the polysilicon and lithographically patterned using a mask for the poly1 layer. After patterning, the polysilicon (poly1) is etched and the remaining PSG is stripped using RIE (**Figure 40g**). Then a second oxide sacrificial layer is deposited and is patterned using different etch masks. For the butterfly gyro, poly1_poly2_via level was used as this provides etch holes in the second oxide down to the poly1 layer. A blanket of this layer was lithographically patterned and etched by RIE to create a double-stacked poly1 and poly2 structure (**Figure 40h**). The poly2 layer was deposited at a thickness of 1.5 μm on top of the poly1 layer and photoresist was also deposited [35]. Then, the layer was lithographically patterned with the seventh mask and etched by the RIE process. The photoresist is then stripped in a solution (**Figure 40i**). The final deposited layer is the metal layer at a thickness of 0.5 μm . This is used for providing electrical connections and bonding. Again, the wafer is lithographically patterned using an etch mask and the metal is deposited and patterned using lift-off (**Figure 40j**). The last step is a sacrificial oxide release (**Figure 40k**). This is performed by immersing the chip in a bath of 49% hydrofluoric acid (HF) at room temperature for 1.5-2 minutes [35]. The chips are immersed in DI water and then alcohol to reduce stiction. Lastly, they are baked for 10 minutes at 110 $^{\circ}\text{C}$.

Design Layout

The butterfly gyro mask CAD file was drawn in L-Edit (Layout Editor) version 2018. The space allocated for this design was 4.75 mm x 4.75 mm. **Figure 42** shows one design of the butterfly gyro. An array of 3 by 3 was created, with minor variations in the geometry. This design consists of four proof masses, two anchors, two paddle beams, a synchronizing beam, two dampers, four sets of electrodes, eight bond pads and eight connections from electrodes to each bond pad. The

electrodes are drawn on poly0 as this layer is fixed and one can apply electrical signals to it. The connections, bond pads and anchors all have been drawn on poly0. The poly0 layer electrodes are used to actuate the device and detect the capacitance change from the proof mass. The proof masses are drawn as double-stacked structures on the poly1 and poly2 layers.

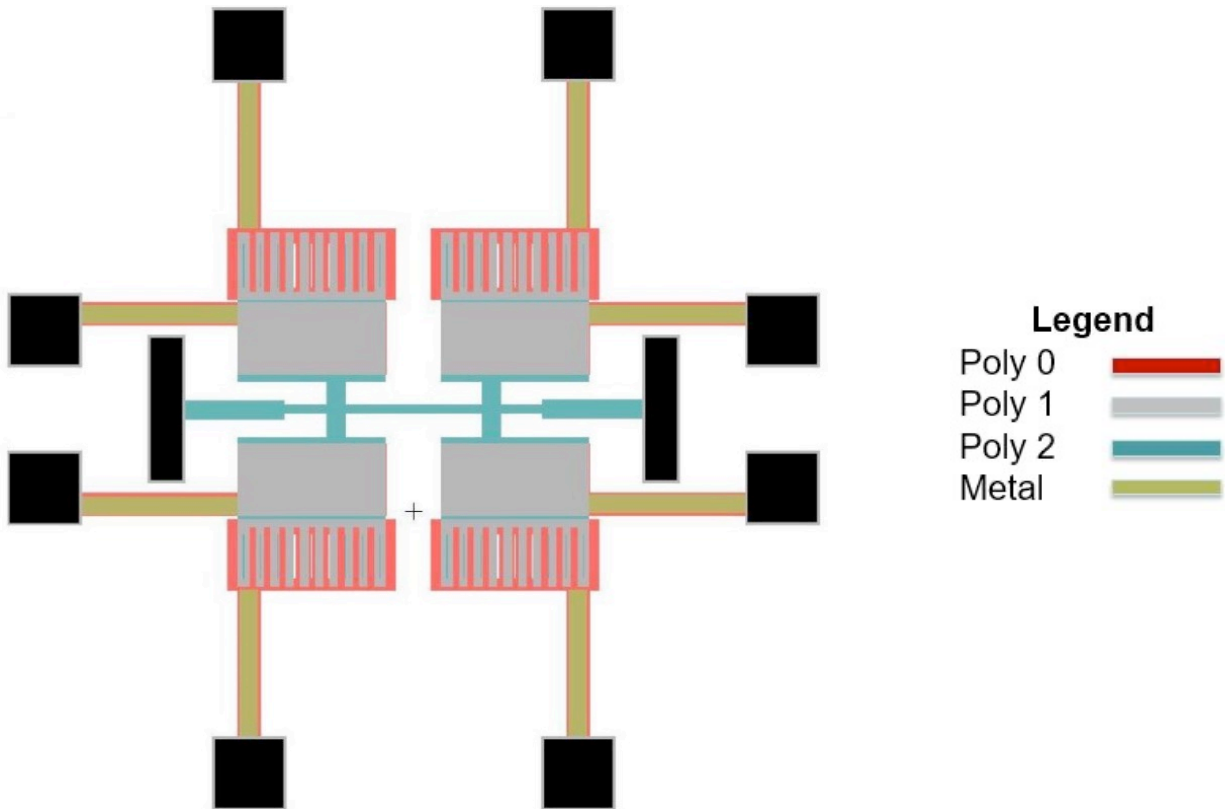


Figure 42. 2D butterfly gyro drawn in L-Edit showing the location of bond pads and connections.

For illustrative purposes, the proof mass is drawn on the poly1 layer while the synchronizing beam, dampers and paddle beams are drawn on the poly2 layer. But in reality, the vibrating structure of the butterfly gyro (proof mass, paddle beams, dampers and synchronizing beam) are a double-stacked structure on poly1 and poly2 combined. The actual structure is drawn on poly2, as this is the top-most structural layer in the topology and, in poly1, there is a blanket layer enclosing poly2. The double structure is made using the poly1_poly2_via layer which strips off the second oxide

(not shown in the figure), eliminating the gap. The metal layer is the top layer, providing connections and bond pads, which supply electrical signals to the electrodes. The anchors and bond pads have turned black in color (**Figure 42**) as they include an anchor1 etch mask. This layer gets rid of the first oxide and is used to fix the components on the substrate.

Figure 43 shows the bonding diagram of the butterfly chip. This includes a 3 by 3 array of the butterfly gyro design. Each design is numbered using alignment markers so it's easier to find under a microscope. The perimeter of the design contains 72 bond pads, which provide connections between the outer electrodes and bond pads from the gyroscope. This is done to make the design packageable and uses an 84-pin grid array (PGA). There are 4 different variations of the butterfly geometry which have been repeated a total of nine times, creating the 3 by 3 array.

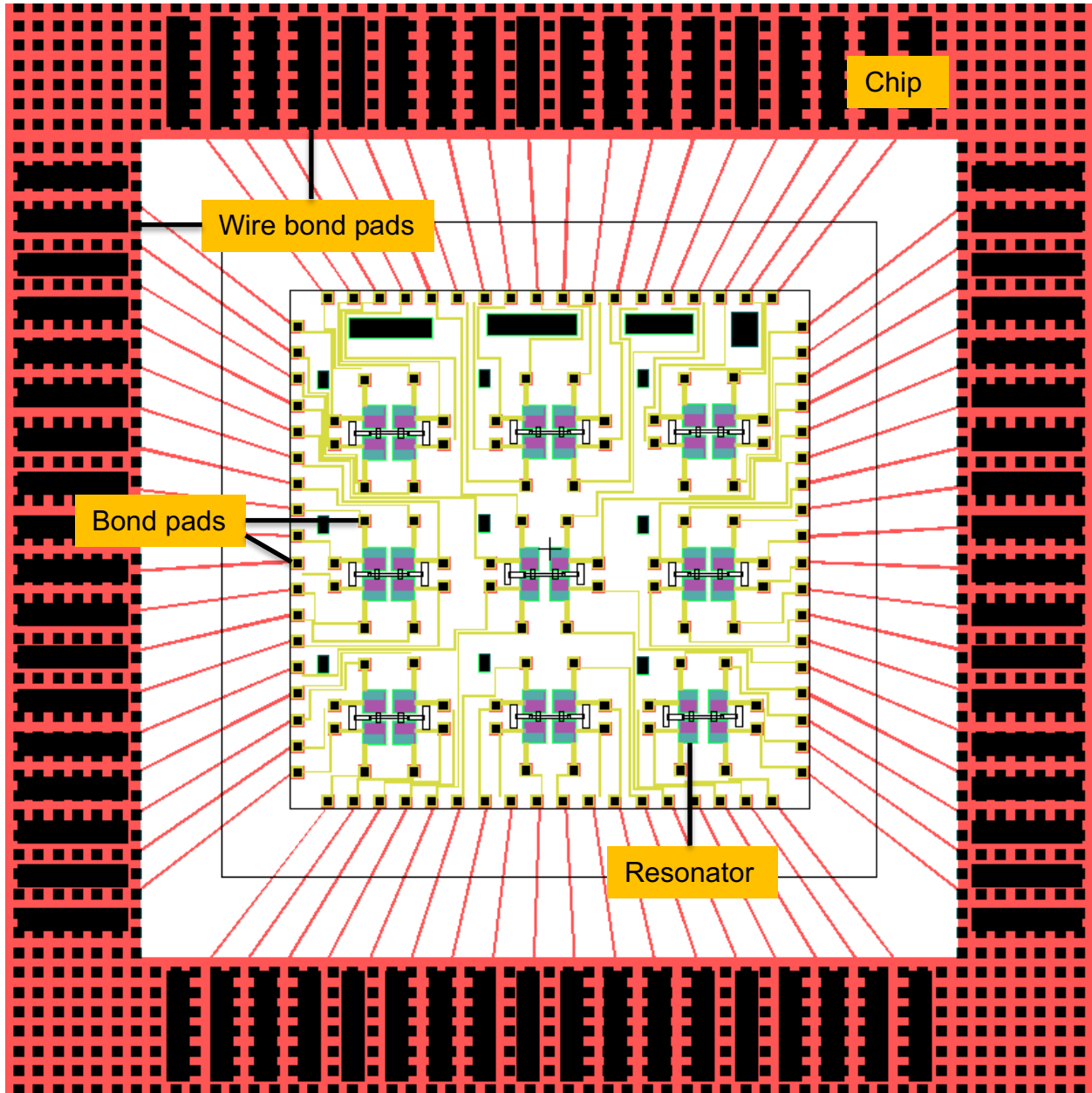
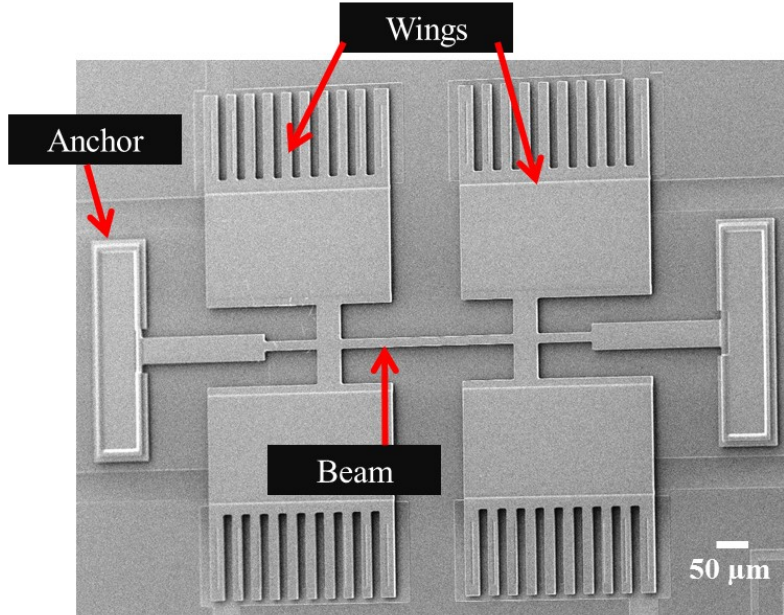


Figure 43. Bonding diagram of the butterfly chip illustrating a total of nine gyros with their respective bond pads and connecting electrodes.

The first geometry drawn is based on the original dimensions designed in COMSOL when doing the eigenfrequency study. Theoretical analysis showed that varying the synchronizing beam resulted in the greatest frequency split, which would affect the performance of the device. For this reason, the second variation in geometry was made to the synchronizing beam for an increased width of 11 μm . Increasing the width could potentially make the structure more stable and robust.

For the third variation in geometry, the number of combs on the proof masses was increased from 10 to 17. This was done because increasing the number of combs increases the electrostatic drive force, as shown in **Figure 28**. This geometry has a slight increase in capacitance as there is more overlap area. The fourth variation included changing the width of the proof mass from 400 to 200 μm . Further analysis demonstrated acceptable frequency split with a decreased proof mass width. A scanning electron microscope (SEM) image of a single gyroscope is shown in **Figure 44** (a) and (b) illustrates the final packaged chip.

(a)



(b)

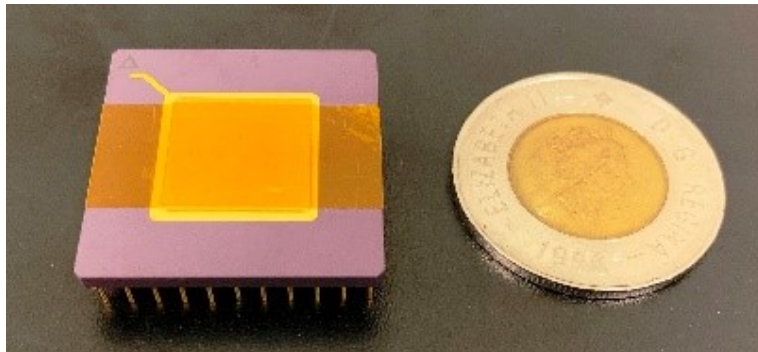


Figure 44. Fabricated butterfly gyro showing (a) a SEM image of one chip and (b) the corresponding packaged gyroscope.

Chapter 4

Experimental Analysis

The butterfly gyro prototype has been designed and developed using the PolyMUMPS process. The gyroscope structure has been characterized using SEM images. The SEM image illustrates high-fidelity fabrication with respect to geometric size as was intended. From the SEM image, one can see that the proof mass and synchronizing beam are suspended and can potentially vibrate. The next step is to investigate the experimental frequency analysis.

Apparatus Used

Experimental characterization and testing of the prototype butterfly gyroscope were performed to capture the dynamic responses of the resonators. The testing verified the theoretical results obtained from the optimized model. This included resonant frequency, quality factor, frequency mismatch and frequency response. The electrostatic drive and sensing setup consisted of a waveform generator (DG4102), spectrum analyzer (RSA507A), lock-in amplifier (HF2LI), two DC power supplies (E3630A, STP3005H), solderless breadboard and oscilloscope (DS1054) for debugging, as shown in **Figure 45**.

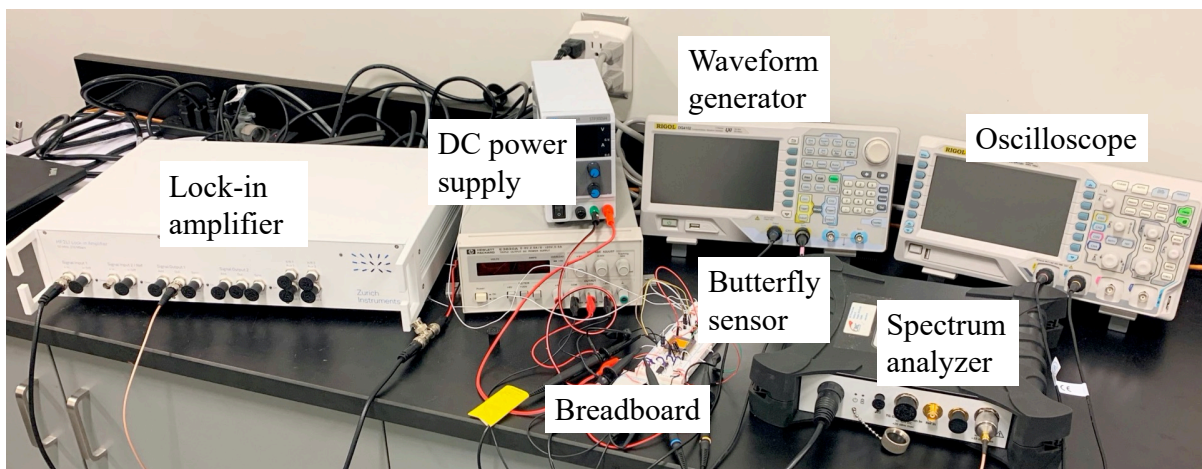


Figure 45. Frequency response test setup that includes two DC power supplies, a waveform generator, a spectrum analyzer, an oscilloscope and a breadboard to interface with the chip.

A waveform generator transmits a signal over a certain range of frequencies and can measure the input-output of the system. The standard waveform includes sine, square, pulse, ramp and harmonics. The maximum frequency on the DG4102 is 100 MHz, with a sampling rate of 500 MSa/s [36]. The spectrum analyzer display receives the signal's amplitude as it varies by frequency. The analyzer shows data in the frequency domain, which is helpful when viewing large and small signals on the same scale. The RSA507A can do real time display of spectrums, with a dynamic range of -160 to +20 dBm [37]. A lock-in amplifier is a digital instrument capable of measuring and extracting signals from a noisy environment. The amplifier can integrate multiple instruments, such as FFTs, plotters, sweepers and software triggers. Oscilloscopes are electronic instruments that graphically display electrical signals in the time domain. They show electrical signals in amplitude vs time. The signals appear as sinusoidal waves in the time domain and, in the frequency domain, they appear as distinct impulses.

Breadboard Electronics

The actuation and detection were accomplished using a breadboard. The breadboard included an actuation and detection circuit. The circuits provided voltages to the electrodes on the resonator chip and simultaneously detected the motion of the proof mass. To build the circuit on the breadboard, the following electrical and electronic components were used:

- (a) Operational amplifiers (OP177 x 2)
- (b) Instrumentation amplifiers (AD620 x 3)
- (c) Resistors (500 k Ω x 3, 10 k Ω x 2, 1 k Ω x 2)
- (d) Capacitors (1 μ F x 2, 10 pF x2)
- (e) Socket for interfacing chip to breadboard
- (f) Jumper wires, scope probes, BNC cables, banana plugs, a BNC splitter and an RF connector.

The actuation circuit consists of two instrumentation amplifiers (AD620), two 500 k Ω and 1 k Ω resistors and two capacitors (1 μ F). A schematic diagram of the circuit is shown in **Figure 46**.

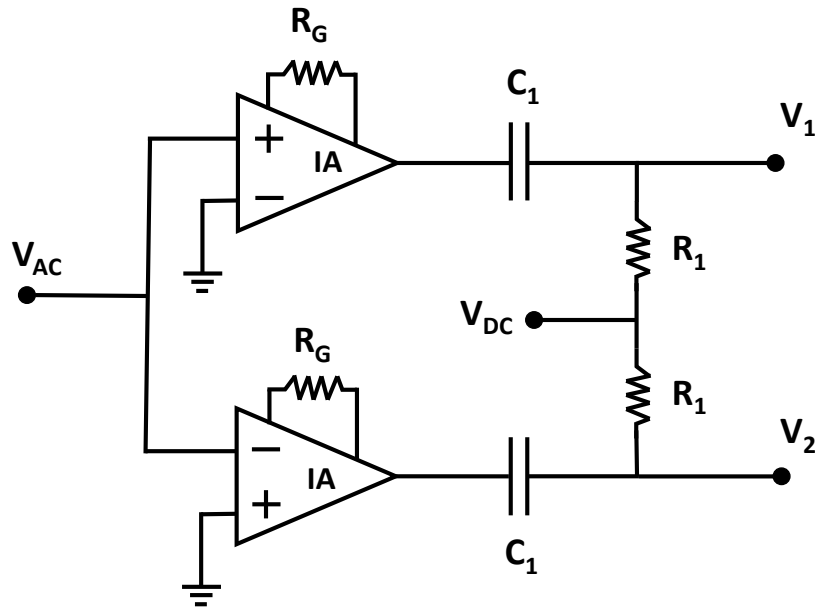


Figure 46. Actuation circuit where $IA = AD620$, $R_G = 500k\Omega$, $R_1 = 1K\Omega$ and $C_1 = 1\mu F$.

The first step in connecting the actuation circuit together on the breadboard is to hook up the rails to become 15 volts and ground. This is provided by one of the power sources which powers the circuit. The next step is to connect the passive components based on the actuation circuit shown in **Figure 47**. Actuation is obtained by mixing the AC and DC voltages and applying this signal to the MEMS device. The AC voltage is delivered by the waveform generator or spectrum analyzer and the DC voltage by the second power source. This applied voltage creates a force on the proof mass that drives it into resonance.

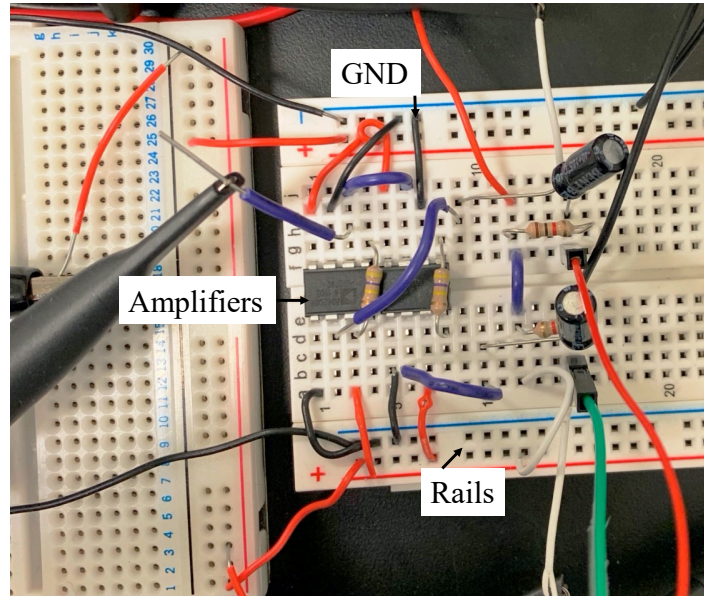


Figure 47. Actuation circuit completed on the breadboard using amplifiers, resistors and capacitors.

The next step is to create the detection circuit on the breadboard. The circuit consists of two operational amplifiers (OP177), one instrumentation amplifier (AD620), a 500 k Ω and two 10 k Ω resistors and two 10 pF capacitors. A schematic diagram of the detection circuit is shown in **Figure 48**.

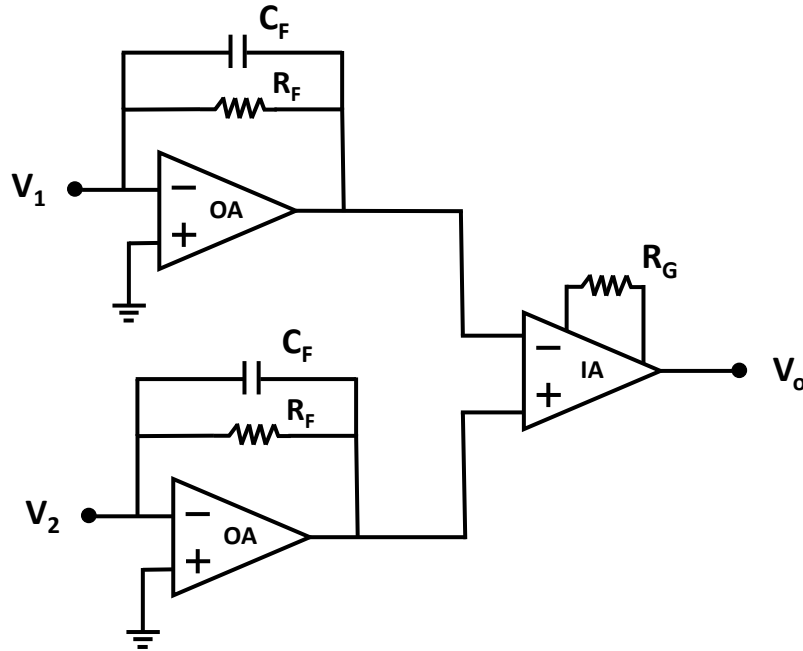


Figure 48. Detection circuit where $OA = OP177$, $IA = AD620$, $R_G = 500k\Omega$, $R_F = 10k\Omega$ and $C_F = 10pF$.

The passive components are connected on the breadboard according to the pin configuration of the amplifiers and then jumper wires are used to connect the components to the rails (**Figure 49**). A parasitic capacitance of the MEMS device is assumed to be 10 pF. Electromechanical amplitude modulation is used where an AC signal is applied to the proof mass with zero DC offset. This is the carrier signal which carries information about the motion of the structure. This signal passes over a variable gap based on the resonator displacement and is then detected using the fixed electrodes. The electrodes output a current that is a function of the carrier signal and motion of the proof mass. This current is converted to a voltage and added to the breadboard. The voltage is then fed back into the lock-in amplifier that extracts the motion of the resonator. After the circuit was completed, the test setup was built.

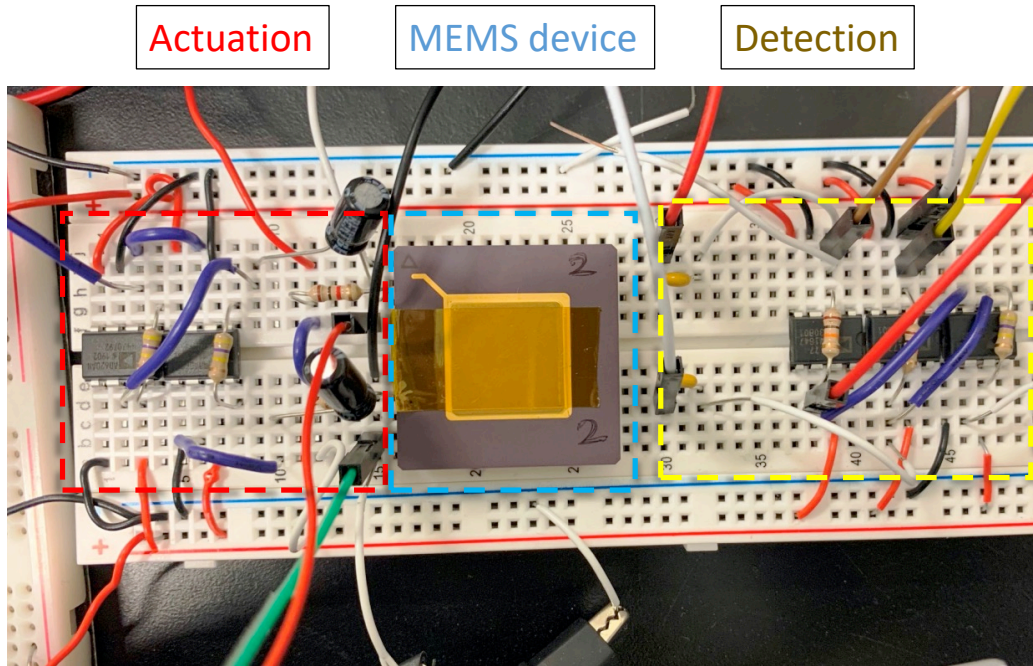


Figure 49. Breadboard implementation illustrating actuation, capacitive detection and MEMS device.

Test Setup

Testing the MEMS device was carried out by connecting external equipment to the breadboard. The first step was to connect the actuation circuit ports with the MEMS device using male-to-male jumper wire. Two wires (V_{A1} & V_{A2}) were needed to excite the proof mass at 180° apart. Then, another two wires (V_{D1} & V_{D2}) were connected from the MEMS device to the detection circuit. Next, the output pin was located on the connection diagram of the AD620 amplifier and a BNC-to-wire cable was used to connect the hole (V_o) to the lock-in amplifier. Another BNC-to-wire cable is used to connect the proof mass of the resonator to the output port on the lock-in amplifier ($V_{CARRIER}$). A spectrum analyzer or a waveform generator can be used to supply the AC voltage (V_{AC}) to the actuation circuit. The spectrum analyzer also receives the demodulated signal (Demod V_o) for the detection of the changing actuation frequency. To supply the DC voltage (V_{DC}) to the resonator, STP3005H was used with five volts DC. Powering the entire circuit (actuation and

detection) was the second power supply, E3630A, with fifteen volts. **Figure 50** shows the setup and the connections within the equipment.

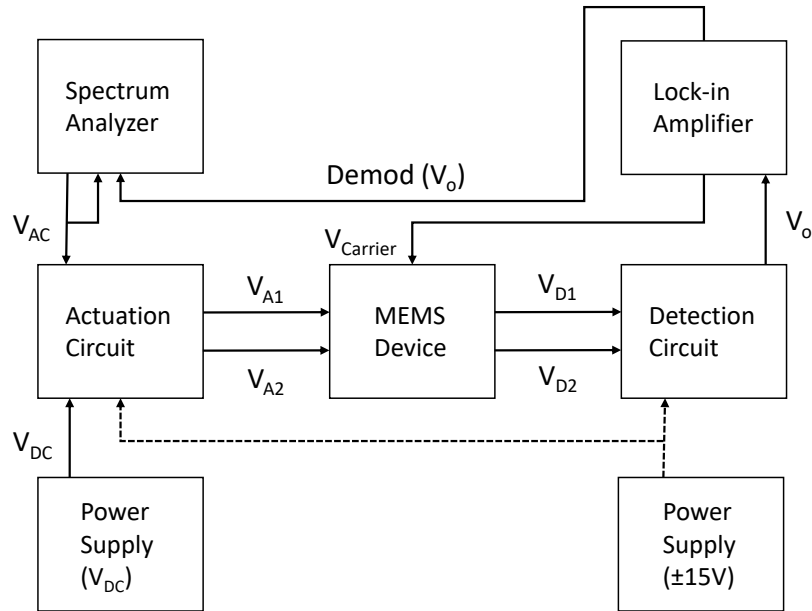


Figure 50. Setup of equipment and connections for the MEMS device.

The four jumper wires used for excitation and detection interface with the MEMS device and breadboard. The resonator includes bond pads on the perimeter of the design that are wire bonded to the outer contact pads of the packaged chip (**Figure 51**). These outer contact pads are connected to the pins that are inserted into the breadboard and this information can be found in the schematics given by the manufacturer. One has to determine the pin locations that correspond to the electrical connections on the MEMS device. Then, the jumper wires interface with the drive and sense pins.

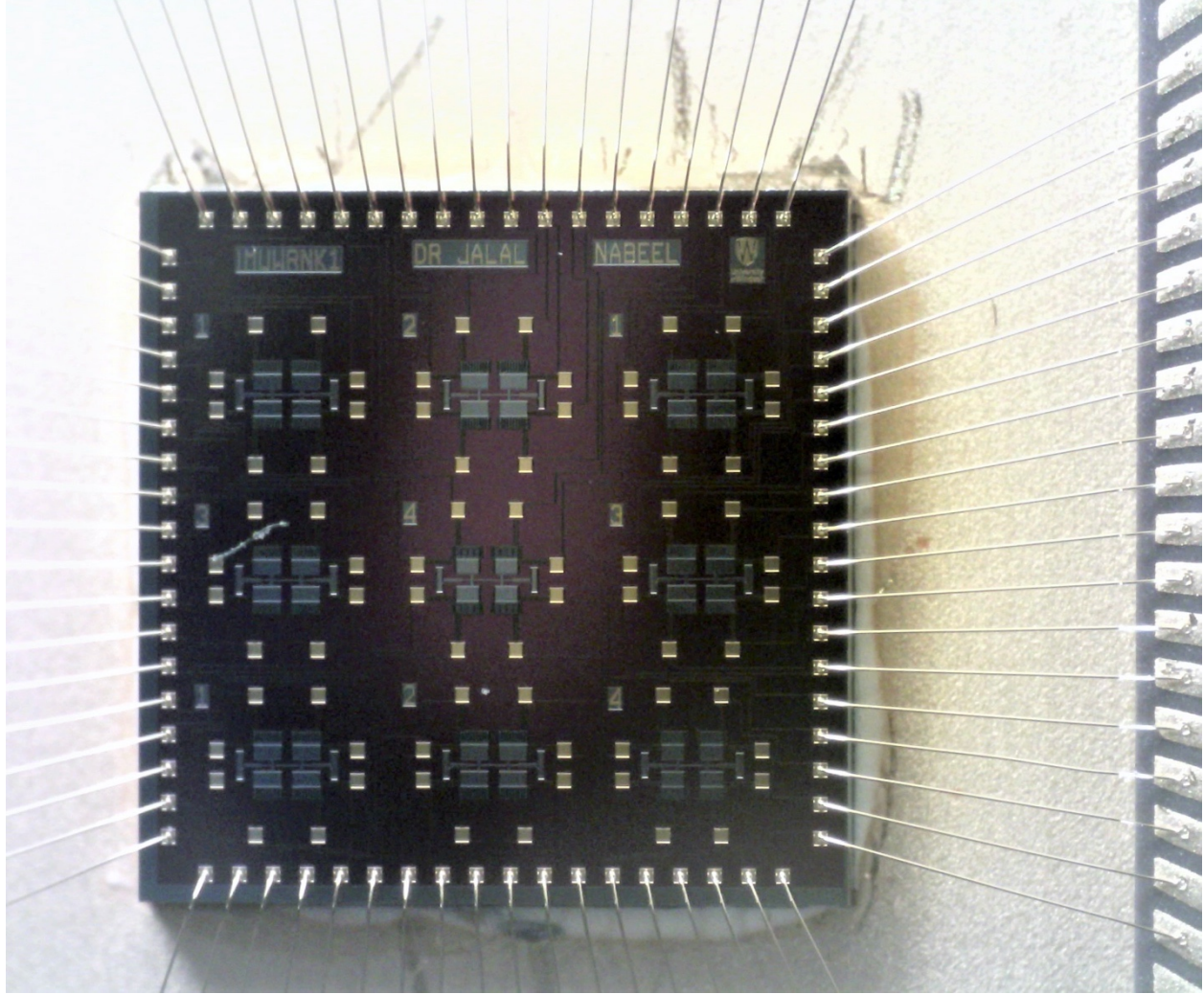


Figure 51. Butterfly chip wire bonded from the bond pads to the outer contact pads.

Probe Station

A mechanical probe station was used to test the device to observe it under an applied voltage, as shown in **Figure 52**. This proved to be a faster and more flexible approach for preliminary testing when compared to the packaged chip on the breadboard.

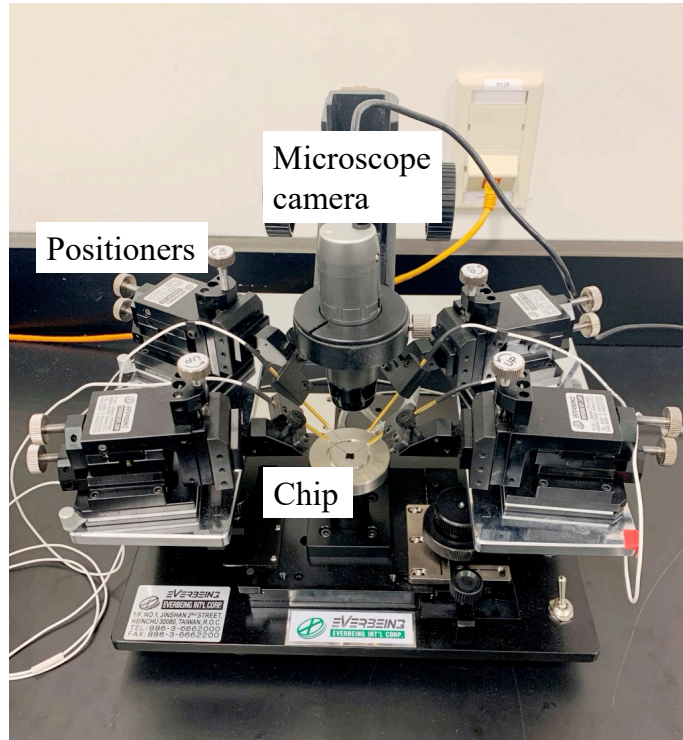


Figure 52. Portable probe station with four positioners, digital microscope camera and butterfly chip sitting on top of the chuck.

The probe station has DC needle probes with four positioners and is equipped with a vacuum pump for the vacuum chuck. The needles are positioned precisely on the semiconductor chip to physically probe the device, as shown in **Figure 53**. This is achieved with the help of a USB microscope camera fixed directly on top of the chuck. Electrical probing is performed by connecting the ends of two of the needles to the waveform generator, with their other ends probed on the electrodes. There are two more needle probes that probe the proof masses, with their other ends connected to the oscilloscope to view the acquired signal.

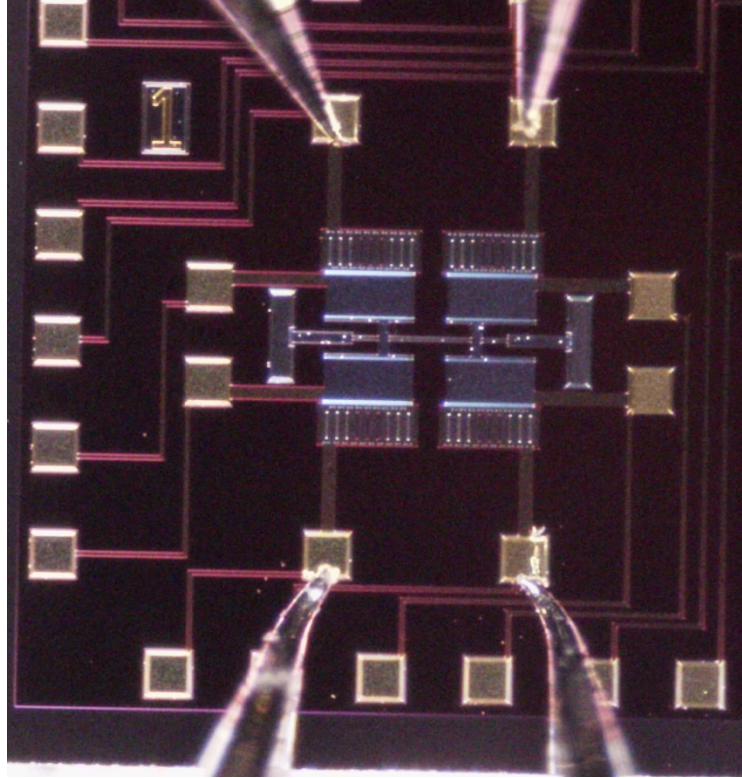


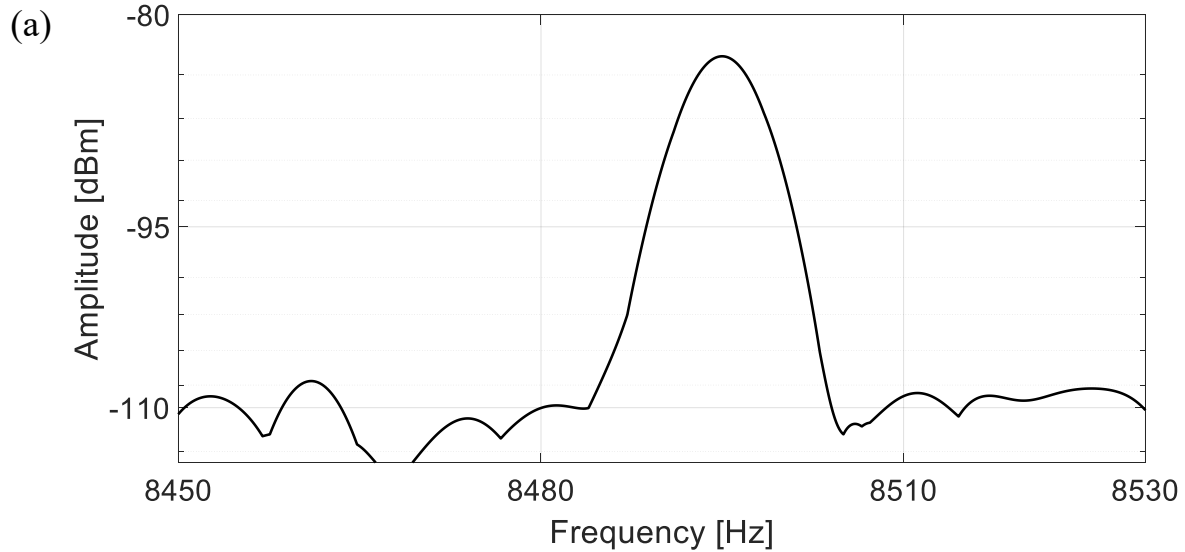
Figure 53. Needles electrically probing the bond pads that are connected to the electrodes.

Response Plots

The frequency response plots illustrate the resonant frequency for the prototype devices. Two prototype designs were tested to compare the experimental frequency split against the split estimated in the model. The spectrum analyzer measured the response from the prototypes by doing a frequency sweep. The optimized model included a thickness of $10\ \mu\text{m}$ for the structural layer. The PolyMUMPS process, however, allows for a double-layered structure thickness of $3.5\ \mu\text{m}$. The eigenfrequency study was then run with the prototype dimension and thickness of $3.5\ \mu\text{m}$. The results were compared, and the frequency split was observed.

The dimensions of prototype 1 included a width and length of proof mass of $400\ \mu\text{m}$, a synchronizing beam width of $11\ \mu\text{m}$, a paddle beam width of $45\ \mu\text{m}$, and a proof-mass-to-

synchronizing-beam distance of 150 μm . The synchronizing beam width was increased by 2 μm , as this value was optimized for the 3.5 μm thickness. The expected frequency split from the model was 195 Hz and the experimental split was 305 Hz. Prototype 2 had similar dimensions as prototype 1, except the synchronizing beam width was increased to 12 μm . The expected frequency split from the model was 220 Hz and the experimental split was 400 Hz. **Figure 54a** shows the drive response of prototype 1 and **Figure 54b** shows the sense mode response. **Figure 55a** shows the drive mode response of the gyro at 8.6 kHz and **Figure 55b** shows the sense mode response at 9.0 kHz.



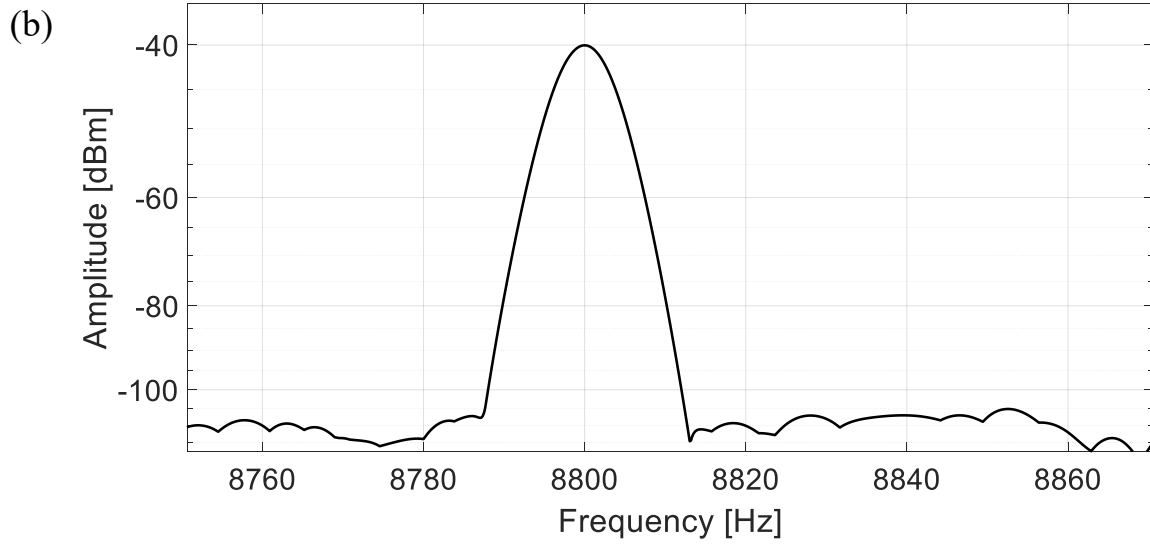
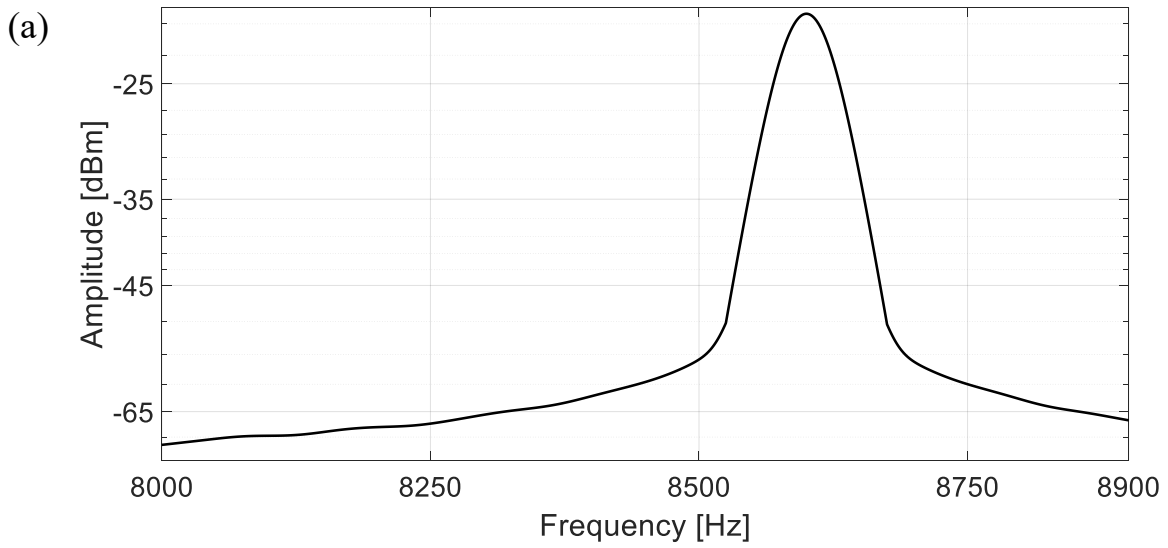


Figure 54. Frequency response of prototype 1 showing (a) drive and (b) sense mode at 8.495 kHz and 8.8 kHz.



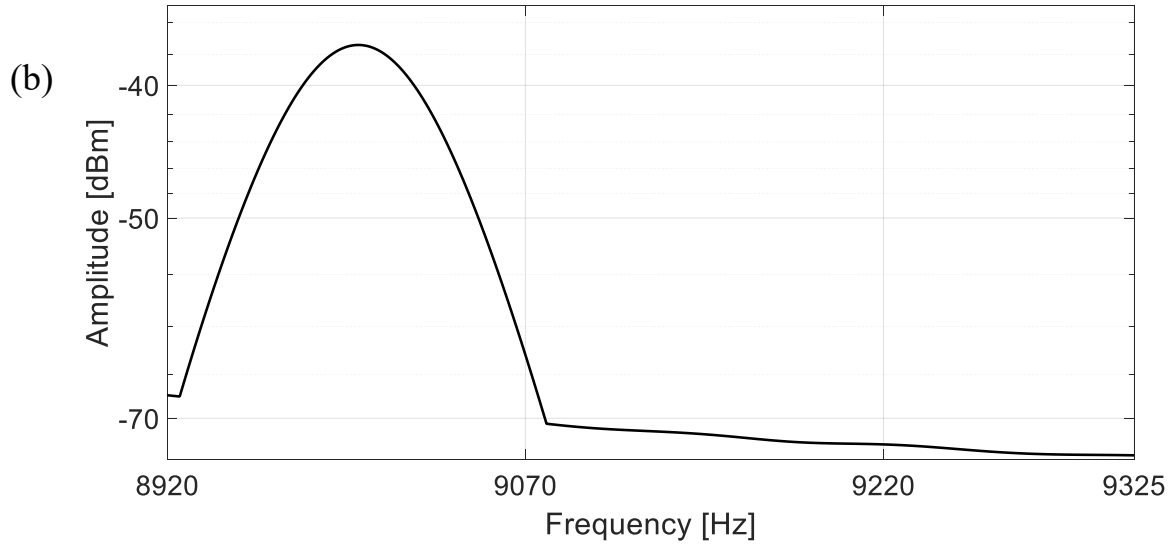


Figure 55. Frequency response of prototype 2 showing drive mode frequency (a) at 8.6 kHz and sense mode frequency (b) at 9.0 kHz.

The Q-factor is calculated for prototype 1 using the formula below:

$$Q = f_0/\Delta f \quad (15)$$

where f_0 is resonant frequency and Δf is the full width at half maximum. The full width at half maximum (FWHM) is the width of the resonance peak between two points on the y-axis, where the power drops to half of the resonance value [38]. On the decibel scale, this corresponds to approximately -3 dB. Evaluating the Q-factor with the formula above requires manual post-processing of the data. The Q-factor for prototype 1 is found to be 906, which was measured under atmospheric pressure. The experimental results have acceptable solutions compared with the model results. The frequency response from the model illustrates a good correlation with the experimental response. The frequency split for prototype 1 and 2 are within limits to the model frequency split, verifying a high fidelity.

Table 8 highlights the frequency summary for the three different studies. The theoretical split is reduced the most for the eigenfrequency study, with a split of 5 Hz. The theoretical and measured

drive and sense frequency for prototype 1 and 2 are relatively close to each other while their splits are farther apart. This could be due to the gyro being tested in atmospheric condition, resulting in performance deviation from the model. The theoretical quality factor for prototype 1 is approximately nine times larger than the measured Q. This could potentially mean the damping is not captured entirely in the model. Damping such as anchor loss, TED and air damping are not included in the model resulting in a high theoretical Q.

Table 8. Frequency summary for the three different studies.

Study	Theoretical frequency [kHz]	Measured frequency [kHz]	Quality factor
Eigenfrequency	Drive: 7.975 Sense 7.970 Split: 5 Hz	-	-
Resonant frequency (Prototype 1)	Drive: 8.24 Sense: 8.05 Split: 190 Hz	Drive 8.5 Sense 8.8 Split: 300 Hz	Theoretical: 8200 Experimental: 906
Resonant frequency (Prototype 2)	Drive: 8.11 Sense: 8.33 Split: 220 Hz	Drive: 8.6 Sense: 9.0 Split: 400 Hz	-

Chapter 5

Conclusion

This thesis explored the design, simulation, fabrication, sensitivity and geometric analysis of the butterfly gyroscope. The model involved the study of stationary, eigenfrequency and electrostatics. The results show an approach to improving a butterfly gyro's performance through structural optimization.

An arbitrary model was developed into the actual model through the variation of various geometrical parameters. This included the butterfly gyro's synchronizing beam, proof mass, paddle beam, overall size and the distance between each component. A modal and frequency analysis study was performed to observe the mode shape and corresponding frequency. The mode shapes illustrated how the sensor would behave in operating conditions and aided in conducting design feasibility. The frequency correlating with the mode shape was optimized in order to increase the sensitivity. The drive and sense modes of operation are of interest. The drive mode oscillator at the drive mode resonant frequency drives the gyroscope into oscillation and, when induced to an external rotation, the gyro is displaced orthogonally to the drive mode and external rotation.

Optimizing the gyroscope's parameters was done with a combination of variables. First, a parametric sweep of each parameter was performed to observe the changing frequency split. Then, two or more parameters were combined to perform a parametric sweep and the frequency split was observed. The combination that produced the lowest frequency split with the correct mode shape was chosen for the final design. The final dimension of the optimized butterfly gyro included a proof mass width and length of 400 μm , a distance between paddle beams of 450 μm , a paddle beam width of 45 μm , a distance between proof mass and synchronizing beam of 150 μm , a synchronizing beam width of 9 μm and an overall gyro size of 1 mm x 1 mm. The structural optimization of the gyroscope resulted in a reduction of the frequency split between the drive and sense modes. Reducing the frequency split led to increasing the sensitivity. The sensitivity increased exponentially as the frequency split decreased. With a frequency split of 10 Hz, a sensitivity of 10^{-12} ($m/^\circ/s$) was observed.

An electrostatic study was performed to ensure the correct mode shape during operation. This study solved the problem of structural mechanics with an applied DC bias. Symmetric and antisymmetric vibrational modes were computed, which corresponded to specific resonant peaks with the presence of an electric field. The forces that drive the resonator into the two modes of operation were calculated using the energy of a capacitor-battery system. A tangential and normal electrostatic force of 4.3 nN and 811 nN were observed, respectively. The maximum displacement from the model of a biased resonator was found to be 26 nm with a pull-in voltage of 21.89 volts.

Fabrication methods were explored and the PolyMUMPS process was chosen to verify the proof of concept. This polysilicon surface micromachining process is commercially available, versatile and cost-effective. The process included three structural layers where two of the layers were vibrating freely and the other one was fixed. The fabrication method allowed for out-of-plane actuation of the proof mass by positioning fixed electrodes at the bottom of the suspended structure. This mechanism proved to be vital, as the proof masses are vibrating both in-plane and out-of-plane.

A frequency response study was performed on the butterfly model, illustrating the optimum operating frequency approximately at the 8 kHz range. Two prototype butterfly resonators were tested against the modeled resonator's frequency. The experimental testing of prototype 1 illustrated a drive and sense frequency of 8.495 and 8.8 kHz with predicted frequencies of 8.24 and 8.05 kHz, respectively. Prototype 2 illustrated an experimental drive and sense frequency of 8.6 and 9.0 kHz with predicted frequencies of 8.11 and 8.33 kHz, respectively. The experimental results show a frequency split of 305 Hz and 400 Hz, while the model illustrated a split of 195 Hz

and 220 Hz, respectively. The experimental Q-factor for prototype 1 was 906 while the predicated Q from the model was 8,200. The analysis and experiments showed the improvement of performance through structural optimization of the butterfly gyroscope.

Future Work

The sensor chip has multiple butterfly resonators that are connected to the outer pads. One butterfly resonator was tested at a time. This research could further explore how one or more simultaneous resonators can improve the performance. The research utilized an extensive approach to finding the optimum geometry for a certain thickness. More research should be done to develop an optimum geometry for varying structural layer thickness. This would be useful in performing an eigenfrequency study where you would observe the theoretical frequency and corresponding mode shape. Continued research should be done to further characterize the gyroscope. The damping model can include anchor loss. This would be the energy dissipated through the anchor and into the substrate and would reduce the Quality factor, thus providing a more accurate overall Q. The bias stability of the gyro can be analyzed by performing an Allan variance analysis. The ARW value would characterize the white noise on the graph at one second. This work will present performance that can be improved upon, compared to industry standards.

References

- [1] D. Senkal, M. J. Ahamed, M. H. A. Ardakani, S. Askari, and A. M. Shkel, “Demonstration of 1 Million Q-Factor on Microglassblown Wineglass Resonators With Out-of-Plane Electrostatic Transduction,” *J. Microelectromechanical Syst.*, vol. 24, no. 1, pp. 29–37, Feb. 2015, doi: 10.1109/JMEMS.2014.2365113.
- [2] M. J. Ahamed, S. I. Gubarenko, R. Ben-Mrad, and P. Sullivan, “A Piezoactuated Droplet-Dispensing Microfluidic Chip,” *J. Microelectromechanical Syst.*, vol. 19, no. 1, pp. 110–119, Feb. 2010, doi: 10.1109/JMEMS.2009.2036866.
- [3] M. J. Ahamed *et al.*, “Continuous Confinement Fluidics: Getting Lots of Molecules into Small Spaces with High Fidelity,” *Macromolecules*, vol. 49, no. 7, pp. 2853–2859, Apr. 2016, doi: 10.1021/acs.macromol.5b02617.
- [4] C. Acar and A. Shkel, *MEMS Vibratory Gyroscopes: Structural Approaches to Improve Robustness*. Springer US, 2009.
- [5] C. Pao, “The importance of IMU Motion Sensors,” *CEVA’s Experts blog*, Nov. 15, 2018. <https://www.ceva-dsp.com/ourblog/what-is-an-imu-sensor/> (accessed Mar. 24, 2020).
- [6] Gaspard Coriolis, “Mémoire sur les équations du mouvement relatif des systemes de corps,” *J. Ecole Polytech.*, vol. 15, p. 142154, 1835.
- [7] P. Rajai, M. Straeten, S. Alirezaee, and M. J. Ahamed, “Binaural Sonar System for Simultaneous Sensing of Distance and Direction of Extended Barriers,” *IEEE Sens. J.*, vol. 19, no. 24, pp. 12040–12049, Dec. 2019, doi: 10.1109/JSEN.2019.2938971.
- [8] D. Senkal, M. J. Ahamed, A. A. Trusov, and A. M. Shkel, “Electrostatic and mechanical characterization of 3-D micro-wineglass resonators,” *Sens. Actuators Phys.*, vol. 215, pp. 150–154, Aug. 2014, doi: 10.1016/j.sna.2014.02.001.
- [9] P. Rajai, M. Straeten, J. Liu, G. Xereas, and M. J. Ahamed, “Modeling of temperature frequency-compensation of doped silicon MEMS resonator,” in *2018 IEEE International Symposium on Inertial Sensors and Systems (INERTIAL)*, Mar. 2018, pp. 1–2, doi: 10.1109/ISISS.2018.8358151.
- [10] N. Khan and M. J. Ahamed, “Design and development of a MEMS butterfly resonator using synchronizing beam and out of plane actuation,” *Microsyst. Technol.*, Dec. 2019, doi: 10.1007/s00542-019-04705-8.
- [11] F. Ou, Z. Hou, T. Miao, D. Xiao, and X. Wu, “A New Stress-Released Structure to Improve the Temperature Stability of the Butterfly Vibratory Gyroscope,” *Micromachines*, vol. 10, no. 2, 2019, doi: 10.3390/mi10020082.

- [12]J. Su, D. Xiao, X. Wang, Z. Chen, and X. Wu, “Vibration sensitivity analysis of the ‘Butterfly-gyro’ structure,” *Microsyst. Technol.*, vol. 20, no. 7, pp. 1281–1290, Jul. 2014, doi: 10.1007/s00542-013-1913-x.
- [13]D. Senkal, M. J. Ahamed, A. A. Trusov, and A. M. Shkel, “Adaptable test-bed for characterization of micro-wineglass resonators,” in *2013 IEEE 26th International Conference on Micro Electro Mechanical Systems (MEMS)*, Jan. 2013, pp. 469–472, doi: 10.1109/MEMSYS.2013.6474280.
- [14]D. Senkal, M. J. Ahamed, A. A. Trusov, and A. M. Shkel, “Demonstration of sub-1 Hz structural symmetry in micro-glassblown wineglass resonators with integrated electrodes,” in *2013 Transducers Eurosensors XXVII: The 17th International Conference on Solid-State Sensors, Actuators and Microsystems (TRANSDUCERS EUROSENSORS XXVII)*, Jun. 2013, pp. 1380–1383, doi: 10.1109/Transducers.2013.6627035.
- [15]A. Simonelli *et al.*, “Rotational motions from the 2016, Central Italy seismic sequence, as observed by an underground ring laser gyroscope,” *Geophys. J. Int.*, vol. 214, no. 1, pp. 705–715, Jul. 2018, doi: 10.1093/gji/ggy186.
- [16]“Top-down, bottom-up fabrication,” *Imgne*, Oct. 28, 2014. <http://imgne.com/2014/10/top-bottom-nanocarbon/> (accessed Jul. 12, 2019).
- [17]G. I. Andersson, N. Hedenstierna, P. Svensson, and H. Pettersson, “A NOVEL SILICON BULK GYROSCOPE,” 1999.
- [18]X. Wang, D. Xiao, Z. Hou, Q. Li, Z. Chen, and X. Wu, “Temperature robustness design for double-clamped MEMS sensors based on two orthogonal stress-immunity structure,” in *2015 IEEE SENSORS*, Nov. 2015, pp. 1–4, doi: 10.1109/ICSENS.2015.7370240.
- [19]X. Xu, D. Xiao, W. Li, Q. Xu, Z. Hou, and X. Wu, “A Dual-Butterfly Structure Gyroscope,” *Sensors*, vol. 17, no. 12, p. 2870, Dec. 2017, doi: 10.3390/s17122870.
- [20]N. Hedenstierna, S. Habibi, S. M. Nilsen, T. Kvisteroy, and G. U. Jensen, “Bulk micromachined angular rate sensor based on the ‘butterfly’-gyro structure,” in *Technical Digest. MEMS 2001. 14th IEEE International Conference on Micro Electro Mechanical Systems (Cat. No.01CH37090)*, Jan. 2001, pp. 178–181, doi: 10.1109/MEMSYS.2001.906509.
- [21]“Halteres,” *Wikipedia*. May 18, 2019, Accessed: Jul. 18, 2019. [Online]. Available: <https://en.wikipedia.org/w/index.php?title=Halteres&oldid=897715081>.
- [22]S. P. Sane, A. Dieudonné, M. A. Willis, and T. L. Daniel, “Antennal Mechanosensors Mediate Flight Control in Moths,” *Science*, vol. 315, no. 5813, pp. 863–866, Feb. 2007, doi: 10.1126/science.1133598.
- [23]COMSOL Inc, “Finite Element Mesh Refinement Definition and Techniques.” <https://www.comsol.com/multiphysics/mesh-refinement> (accessed Apr. 03, 2020).

- [24] COMSOL Inc, “COMSOL Multiphysics Reference Manual, version 5.3a.” 2017.
- [25] D. Xiao, S. Cao, Z. Hou, Z. Chen, X. Wang, and X. Wu, “Enhanced sensitivity in a butterfly gyroscope with a hexagonal oblique beam,” *AIP Adv.*, vol. 5, no. 4, p. 041331, Mar. 2015, doi: 10.1063/1.4916587.
- [26] Md. Imrul Kaes, D.S-K Ting, and Mohammed Jalal Ahamed, “Modeling Of Structural And Environmental Effects On Microelectromechanical (MEMS) Vibratory Gyroscopes,” in *CSME International Congress 2018*, Toronto, ON, May 2018, doi: 10.25071/10315/35238.
- [27] “Analysis and Design Principles of MEMS Devices - 1st Edition.”
<https://www.elsevier.com/books/analysis-and-design-principles-of-mems-devices/bao/978-0-444-51616-9> (accessed Jul. 25, 2019).
- [28] C. Liu, *Foundations of MEMS*, 2nd ed. Upper Saddle River, NJ, USA: Prentice Hall Press, 2011.
- [29] I. Khan and R. B. Mrad, “Development of a MEMS repulsive actuator for large out-of-plane force,” *J. Micromechanics Microengineering*, vol. 24, no. 3, p. 035022, Feb. 2014, doi: 10.1088/0960-1317/24/3/035022.
- [30] A. Darvishian, T. Nagourney, J. Y. Cho, B. Shiari, and K. Najafi, “Thermoelastic Dissipation in Micromachined Birdbath Shell Resonators,” *J. Microelectromechanical Syst.*, vol. 26, no. 4, pp. 758–772, Aug. 2017, doi: 10.1109/JMEMS.2017.2715319.
- [31] A. Darvishian, B. Shiari, J. Y. Cho, T. Nagourney, and K. Najafi, “Anchor Loss in Hemispherical Shell Resonators,” *J. Microelectromechanical Syst.*, vol. 26, no. 1, pp. 51–66, Feb. 2017, doi: 10.1109/JMEMS.2016.2636080.
- [32] G. Sosale, S. Prabhakar, L. G. Frechette, and S. Vengallatore, “A Microcantilever Platform for Measuring Internal Friction in Thin Films Using Thermoelastic Damping for Calibration,” *J. Microelectromechanical Syst.*, vol. 20, no. 3, pp. 764–773, Jun. 2011, doi: 10.1109/JMEMS.2011.2140357.
- [33] A. Darvishian, B. Shiari, G. He, and K. Najafi, “Effect of substrate thickness on quality factor of mechanical resonators,” in *2015 IEEE International Symposium on Inertial Sensors and Systems (ISISS) Proceedings*, Mar. 2015, pp. 1–4, doi: 10.1109/ISISS.2015.7102379.
- [34] W. E. Newell, “Miniaturization of Tuning Forks,” *Science*, vol. 161, no. 3848, pp. 1320–1326, Sep. 1968, doi: 10.1126/science.161.3848.1320.
- [35] A. Cowen, B. Hardy, R. Mahadevan, and S. Wilcenski, “PolyMUMPs Design Handbook,” *MEMSCAP Inc*, no. rev. 13.0, p. 44, 2011.
- [36] Rigol Technologies Inc, “DG4000 Series Function/Arbitrary Waveform Generator - User guide.” 2014.

[37]“RSA500 Series Real Time Spectrum Analyzers | Tektronix.” <https://www.tek.com/spectrum-analyzer/rsa500-series> (accessed Nov. 18, 2019).

[38]R. Paschotta, “Q Factor,” *Photonics Encyclopedia*. https://www.rp-photonics.com/q_factor.html (accessed Nov. 25, 2019).

Vita Auctoris

NAME: Nabeel Khan
PLACE OF BIRTH: Aligarh, India
YEAR OF BIRTH: 1995
EDUCATION: Yanbu International School, Saudi Arabia, 2013

University of Windsor, BAsC, Windsor ON, 2017

University of Windsor, MAsC, Windsor ON, 2020

PUBLICATIONS:

Conference papers, poster and journal paper

1. Jiewen Liu, Joshua. Jaekel, Dharamdeo Ramdani, Nabeel Khan, David S-K. Ting, and Mohammed Jalal Ahamed, "Effect of geometric and material properties on thermoelastic damping (TED) of 3D hemispherical inertial resonator," ASME 2016, IMECE, Phoenix, USA.
2. Matthew Straeten, Nabeel Khan, Matthew Shamoan and Mohammed Jalal Ahamed, "MEMS based sensor fusion enabling inertial navigation without GPS," IEEE Inertial open poster presentation 2019, Naples, FL.
3. Payman Rajai, Nabeel Khan, Mohammed Jalal Ahamed, "Modeling of nonlinear oscillations of doped lame mode MEMS silicon resonator," 6th IEEE International Symposium on Inertial Sensors and Systems (INERTIAL) 2019, pp 1-3, doi: 10.1109/ISISS.2019.8739289, Naples FL.
4. N. Khan, M.J. Ahamed, "Design and development of a MEMS butterfly resonator using synchronizing beam and out of plane actuation," *Microsyst Technol.*, vol. 26, no. 5, pp. 1643-1652, May 2020, <https://doi.org/10.1007/s00542-019-04705-8>.